

# Novel CoFe<sub>2</sub>P<sub>x</sub> derived from CoFe<sub>2</sub>O<sub>4</sub> for efficient peroxyomonosulfate activation: Switching the reaction route and suppressing metal leaching

Dingxue Gao, Yirui Lu, Yupeng Chen, Mengyuan Bao, Nan Xu\*

*Shenzhen Engineering Research Center for Nanoporous Water Treatment Materials, School of Environment and Energy, Peking University Shenzhen Graduate School, Shenzhen 518055, China*



## ARTICLE INFO

### Keywords:

Bimetallic phosphides  
Peroxyomonosulfate  
Sulphachloropyridazine sodium  
Cobalt leaching  
Ring-opening products

## ABSTRACT

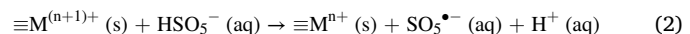
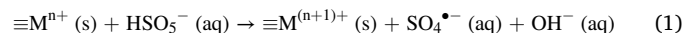
In this study, bimetallic phosphides were reported to be novel, efficient, and stable activators of peroxyomonosulfate (PMS). CoFe<sub>2</sub>P<sub>x</sub> was synthesized by phosphorization of CoFe<sub>2</sub>O<sub>4</sub> and applied in PMS activation for sulphachloropyridazine sodium (SCP) degradation. The SCP removal reached up to 94.2% in 30 min, with a reaction rate of 0.090 min<sup>-1</sup>. Particularly, CoFe<sub>2</sub>P<sub>x</sub> exhibited much lower cobalt ion leaching (0.082 mg L<sup>-1</sup>) than the reported cobalt-containing catalysts, due to the more intimate Co-Fe interaction and the surrounding of metals by phosphorus. Different from the free radical pathway in CoFe<sub>2</sub>O<sub>4</sub>/PMS system, a radical-nonradical coupling process was detected in CoFe<sub>2</sub>P<sub>x</sub>/PMS system, which was confirmed by quenching tests, electron paramagnetic resonance (EPR) measurements, and transformation intermediate analyses. Moreover, CoFe<sub>2</sub>P<sub>x</sub> demonstrates favorable durability for PMS activation and potential practicability for realistic wastewater treatment. This work provides new insights for rational design and mechanism exploration of transition-metal phosphides (TMPs) in the environmental catalysis field.

## 1. Introduction

Sulfate radical (SO<sub>4</sub><sup>•-</sup>)-based advanced oxidation processes (SR-AOPs) have been recognized as a powerful technology for the remediation of contaminated waters. Compared with conventional hydroxyl radical (•OH), SO<sub>4</sub><sup>•-</sup> shows higher oxidizing ability (2.5–3.1 V vs 1.8–2.7 V for •OH [1,2]), longer half-life (30–40 μs vs < 1 μs for •OH [3, 4]) and more robust pH adaptability (pH = 2–9 [5]). Moreover, the reaction of SO<sub>4</sub><sup>•-</sup> with organic compounds shows different pathway and kinetics from that of •OH [6], which provides an alternative degradation mechanism. Generally, SO<sub>4</sub><sup>•-</sup> is produced by the activation of peroxyomonosulfate (PMS) or peroxydisulfate (PDS). Therefore, a low-cost and highly efficient activator is the key for the implementation of SR-AOPs.

Transition-metal-based heterogeneous catalysts, such as bimetallic oxides [7], layered double hydroxides [8] and metal-organic frameworks (MOFs) [9], could effectively activate PDS or PMS without requiring energy input and have been extensively investigated. SO<sub>4</sub><sup>•-</sup> was generated through Eq. 1 accompanied with oxidation of  $\equiv M^{n+}$ . To complete catalytic cycle,  $\equiv M^{(n+1)+}$  was further reduced by another PMS molecule (Eq. 2), which is also the rate-determining step of PMS activation [10]. Among various transition-metal-based heterogeneous

catalysts, cobalt-based catalysts have received more attention. Unlike most other metals, the reduction potential of Co(III)/Co(II) is 1.81 V [11], which lies exactly between the reduction potentials of HSO<sub>5</sub><sup>-</sup>/SO<sub>4</sub><sup>•-</sup> (2.5–3.1 V) and HSO<sub>5</sub><sup>-</sup>/SO<sub>5</sub><sup>2-</sup> (1.1 V), thermodynamically favors the reduction of Co(III), and ensures the formation of a rapid catalytic cycle [12]. In addition, some of the cobalt-based catalysts have specific magnetic properties, providing the feasibility of easy separation and recycling use at the end of reaction [11,13]. However, cobalt leaching is a problem that has not been effectively addressed. It occurs in almost all reported cobalt-based catalysts, leading to not only the reduction of active components but also secondary pollution [14]. Thus, it is most desirable to develop a highly efficient and particularly stable cobalt-based heterogeneous catalyst.



In previous studies, the interactions between cobalt element and the surrounding environment were used to reduce the leaching of cobalt ions in the reaction system, including the preparation of cobalt-containing [15], cobalt-supported [16], cobalt-encapsulated [17] and cobalt-coordinated [18] catalysts. However, most of these strategies are

\* Corresponding author.

E-mail address: [xunan@pkusz.edu.cn](mailto:xunan@pkusz.edu.cn) (N. Xu).

limited to the modification of cobalt oxides or cobalt complexes. New strategies to reduce cobalt leaching still need to be explored.

Transition-metal phosphides (TMPs) have been extensively applied in semiconductors, photocatalysis and electrocatalysis, owing to their low fabrication cost, high conductivity and structural stability. Recently, mono-metallic phosphides ( $M_xP$ ), including  $CoP$  [19],  $Fe_xP$  [20] and  $Cu_3P$  [21], were creatively employed as heterogeneous catalysts in AOPs, and achieved infusive performance in elimination of organic contaminants. However, few studies have focused on the catalytic ability of multi-metallic phosphide for common oxidant activation. Meanwhile, multi-metallic phosphide possessed enhanced activity for oxygen evolution reaction due to the synergistic effect between multiple metals [22]. Therefore, we conceive that multi-metallic phosphide would exhibit excellent catalytic performance in SR-AOPs. Furthermore, in addition to  $SO_4^{2-}$  and  $^{\bullet}OH$ ,  $O_2^{2-}$  and  $^{\bullet}O_2$  were identified in  $Fe_xP/PMS$  system [20], that was sharply different from classic metal oxide system in which  $SO_4^{2-}$  and  $^{\bullet}OH$  were the primary free radicals. Thus, comparison between the activation mechanisms of PMS by metal oxides and phosphides is also worth investigating.

In this work,  $CoFe_2P_x$  was prepared via a three-step method, and employed to activate PMS. Sulphachloropyridazine sodium (SCP), a representative sulfonamide, was selected as the model pollutant, due to its strong acute toxicity, wide distribution, and resistance to conventional bioremediation [23]. The effects of various operating parameters on the catalytic performance of  $CoFe_2P_x$  were evaluated. As expected,  $CoFe_2P_x$  showed high activity and durability for SCP degradation with low cobalt leaching. The catalytic performance and mechanism of PMS activation by  $CoFe_2P_x$  and  $CoFe_2O_4$  precursor were compared, which exhibited obvious differences. Finally, the SCP transformation products were identified and the degradation pathway was proposed.

## 2. Materials and methods

### 2.1. Chemicals and materials

Unless otherwise specified, all chemicals and reagents were of analytical grade and used without further purification. Detailed information is listed in [Text S1 of the Supplementary Information](#).

### 2.2. Catalyst preparation

The catalyst was synthesized according to a previously reported protocol with slight modification [24].

Synthesis of CoFe-MOF: CoFe-MOF was prepared using a hydrothermal method. Specifically, 0.5 mmol of  $Co(NO_3)_2 \cdot 6H_2O$ , 1.0 mmol  $Fe(NO_3)_3 \cdot 9H_2O$ , 0.7 mmol 1,3,5-benzenetricarboxylic acid (BTC), and 1 g polyvinylpyrrolidone (PVP, molecular weight: 58,000) were dissolved in 30 mL N,N-dimethylformamide (DMF). After stirring for 6 min, the solution was transferred to a Teflon-lined stainless autoclave (100 mL) and heated at 150 °C for 6 h. The brown precipitate was collected by centrifugation, washed three times with DMF and ethanol, dried at 80 °C for 24 h, and ground into powder. Co-MOF and Fe-MOF were prepared using 1.5 mmol of  $Co(NO_3)_2 \cdot 6H_2O$  and  $Fe(NO_3)_3 \cdot 9H_2O$ , respectively.

Preparation of  $CoFe_2O_4-n$ : The CoFe-MOF was calcined in a muffle furnace (GWL-1400XB, Luoyang Juxing Kiln Co., Ltd., China) at 450, 650 and 850 °C for 2 h with a ramp rate of 7 °C min<sup>-1</sup> to form  $CoFe_2O_4-n$  ( $n = 1, 2, 3$  for 450 °C, 650 °C, 850 °C, respectively). Pure  $Co_3O_4$  and  $Fe_2O_3$  were obtained by calcining Co-MOF and Fe-MOF at 450 °C, respectively.

Preparation of  $CoFe_2P_x-n$ :  $CoFe_2P_x-n$  was synthesized by low temperature phosphorization. Briefly, 50 mg of  $CoFe_2O_4-n$  and 1.0 g  $NaH_2PO_2$  were placed at two sides of a semi-enclosed porcelain boat with  $NaH_2PO_2$  at the upstream side in the tube furnace. Before heating, the tube was purged with Ar for 20 min. Subsequently, the samples were heated at 350 °C for 2 h at a heating rate of 2 °C min<sup>-1</sup> in an Ar atmosphere (35 standard cubic centimeter per minute (scm)).  $CoP$  and

$FeP$  were obtained via the same synthesis process but replacing  $CoFe_2O_4-n$  with  $Co_3O_4$  and  $Fe_2O_3$ , respectively.

### 2.3. Characterization of the catalysts

The surface morphology and elemental distribution of catalysts were examined with a Zeiss Sigma 300 scanning electron microscope (SEM) (Carl Zeiss, Germany) equipped with an energy dispersive X – ray fluorescence spectrometer (EDX) (SmartEDX, Carl Zeiss, Germany). The microstructure of catalysts was observed with a FEI Tecnai G2 F20 transmission electron microscopy (TEM, HT7700, Japan). The bulk chemical compositions of catalysts were determined by X-ray fluorescence (XRF, Bruker S6 JAGUAR, Germany). X-ray diffraction (XRD) patterns were collected on a Bruker D8 Discover micro X-ray diffractometer (Bruker Co., Germany) with Cu K $\alpha$  X radiation (45 kV, 100 mA), 0.02° of measurement step and 0.05 s of channel integration time. Fourier transform infrared (FT-IR) spectra were taken in KBr pressed pellets on a Thermo Scientific Nicolet iS50 FT-IR spectrometer (Thermo Fisher, Madison, USA). Raman spectra were recorded on a LabRAM HR800 spectrometer (Horiba Jobin Yvon, France) employing 785, 785, and 532 nm laser for CoFe-MOF,  $CoFe_2O_4-1$ , and  $CoFe_2P_x-1$ , respectively. X-ray photoelectron spectroscopy (XPS) measurements were carried out on an EscaLab 250Xi XPS system (Thermo Fisher Scientific Inc., USA), and the binding energies of all the elements were calibrated with the C 1s peak at 284.8 eV. The specific surface area and pore structure were obtained on a BELSORP-max (BEL, Osaka, Japan) instrument.

### 2.4. Experimental procedure and analytical methods

Unless specifically noted, all the experiments were carried out in a cylindrical glass reaction vessel of 500 mL capacity at 25 °C. Typically, the required amount of catalyst was added to 200 mL of SCP solution with a concentration of 10 mg L<sup>-1</sup>. Then, the solution was shaken at a rotation speed of 120 rpm, a known concentration of PMS was added to the solution, and the initial pH was adjusted to 6.9 using 0.1 mol L<sup>-1</sup> NaOH to initiate the reaction. At different time intervals, samples were withdrawn from the reactor and filtered through 0.45 μm polyvinylidene fluoride (PVDF) syringe filters (SCAA-109, Anpel, China). The filtration exerted a negligible impact on the SCP concentration, which has been confirmed in our previous work [25]. Exactly 0.9 mL of the filtered sample was injected into a 2 mL amber glass vial containing 0.1 mL of  $Na_2S_2O_3$  (0.1 mol L<sup>-1</sup>) to inhibit the reaction of any residual ROS. All the samples were stored at 4 °C and analyzed within 12 h.

The effects of potential influential factors, including pH, inorganic ions, and humic acid, were investigated by changing the parameters accordingly. For reusability tests, the used catalyst was collected by magnetic separation and dried out at 60 °C overnight. Due to the inevitable trace loss of catalyst during the recovery process, six parallel experiments were set up at the first run to ensure that the dosage of catalyst was constant in the subsequent runs.

The methods related to the determination of SCP and leached Co and Fe ions, the identification of ROS and SCP degradation intermediates are shown in [Text S2](#).

## 3. Results and discussion

### 3.1. Characterization of the catalyst

The morphology evolution of the as-synthesized materials was evaluated by SEM and TEM. As shown in [Fig. S1a and d](#), CoFe-MOF was wrapped in a thin layer, which was formed during the drying process of DMF and PVP (the boiling points of DMF and PVP are 153.0 °C and 217.6 °C, respectively). After calcination, the thin layer disappeared, and the generated  $CoFe_2O_4-1$  showed a spherical morphology with a diameter around 10–25 nm ([Fig. S1b and e](#)). After phosphorization, the

obtained  $\text{CoFe}_2\text{P}_x\text{-}1$  inherited the morphology of its oxide precursor but with diameters increased to 15–40 nm (Fig. S1c and f), which was attributed to thermal expansion during heating [19]. The EDX analysis confirmed the presence of Fe, Co, P in  $\text{CoFe}_2\text{P}_x\text{-}1$ , and the elemental mapping (Fig. S1g) displayed the homogeneous distribution of the elements. The weight ratio of Co: Fe: P is estimated to be 1: 2: 1.5 via XRF analysis (Table S1), corresponding to the molar ratio of 1: 2.1: 2.8, which is similar to the previously reported material synthesized as water-splitting catalyst [26].

The crystallographic structure and phase purity of the as-synthesized materials were identified by XRD analysis (Fig. 1a). The pattern of CoFe-MOF showed an amorphous nature. After calcination treatment in air, the distinct peaks at  $30.2^\circ$ ,  $35.6^\circ$ ,  $43.3^\circ$ ,  $53.5^\circ$ ,  $57.2^\circ$ ,  $62.7^\circ$ ,  $71.4^\circ$ , and  $74.0^\circ$  well matched those of  $\text{CoFe}_2\text{O}_4$  phase (JCPDS card No. 02-1045), suggesting the successful conversion of CoFe-MOF into  $\text{CoFe}_2\text{O}_4\text{-}1$  with a high purity. After phosphorization, the diffraction peaks were obviously different from those of cobalt-iron phosphate [27], but the same as those of CoP, located between the characteristic peaks of CoP and FeP, indicating the formation of cobalt-iron phosphide, i.e.  $\text{CoFe}_2\text{P}_x\text{-}1$ . Furthermore, the XRD pattern of  $\text{CoFe}_2\text{P}_x\text{-}1$  was consistent with the previous report [28].

Fig. 1b shows the FT-IR spectra of the as-synthesized materials. The broad band at around  $3440 \text{ cm}^{-1}$  existing in all samples was ascribed to the O-H stretching of surface hydroxyl groups. The stretching vibrations of C-H, C=C, Co-O and Fe-O at  $2921$ ,  $1376$ ,  $663$ , and  $580 \text{ cm}^{-1}$  indicated the successful synthesis of CoFe-MOF [29]. The C=N bond ( $1660 \text{ cm}^{-1}$ ) and C-N bond ( $1102 \text{ cm}^{-1}$ ) were due to the remaining DMF and PVP.

After calcination, the characteristic peaks of the organic ligands disappeared. A strong peak related to Fe-O bond appeared at  $584 \text{ cm}^{-1}$ , which is the representative adsorption peak of  $\text{CoFe}_2\text{O}_4$  [30]. In the FT-IR spectrum of  $\text{CoFe}_2\text{P}_x\text{-}1$ , a band around  $800$ – $1200 \text{ cm}^{-1}$  and a peak at  $545 \text{ cm}^{-1}$  were observed, which were attributed to the bending vibration from the  $\text{PO}_4^{3-}$  group [31]. The formation of phosphate in phosphide is inevitable, due to the inhomogeneous gas-solid interfacial reaction between  $\text{PH}_3$  generated by the heating of phosphorus source and metal oxides during the preparation [32]. Meanwhile, TMPs tend to be oxidized in air because of its high surface energy [33,34].

Raman spectra were adopted to further characterize the crystal structure (Fig. 1c). The Raman spectroscopy of  $\text{CoFe}_2\text{O}_4\text{-}1$  showed peaks at  $192$  (F2 g),  $303$  (F2 g),  $474$  (Eg),  $611$  (F2 g) and  $678 \text{ cm}^{-1}$  (A1 g), which are completely in agreement with the previously reported spectra [35]. Abundant vibration peaks appeared in the Raman spectrum of  $\text{CoFe}_2\text{P}_x\text{-}1$ , and significant differences were observed between the Raman spectra of  $\text{CoFe}_2\text{O}_4\text{-}1$  and  $\text{CoFe}_2\text{P}_x\text{-}1$ , implying that the oxide was successfully converted into phosphide.

The wide-scan XPS survey (Fig. 1d) showed that the peak intensities of Co 2p and Fe 2p in CoFe-MOF were unrecognizable, which further confirmed that CoFe-MOF was wrapped by the layer composed of DMF and PVP. After calcination, the peak of N 1s disappeared, which was consistent with the fate of N-containing groups in FT-IR spectra. After phosphorization, the peak strength of O 1s significantly decreased and a P 2p peak appeared, indicating the formation of phosphide. As displayed in Fig. S2a, the high-resolution Co 2p spectrum of  $\text{CoFe}_2\text{P}_x\text{-}1$  was deconvoluted into two major spin-orbit doublets. The first doublet at

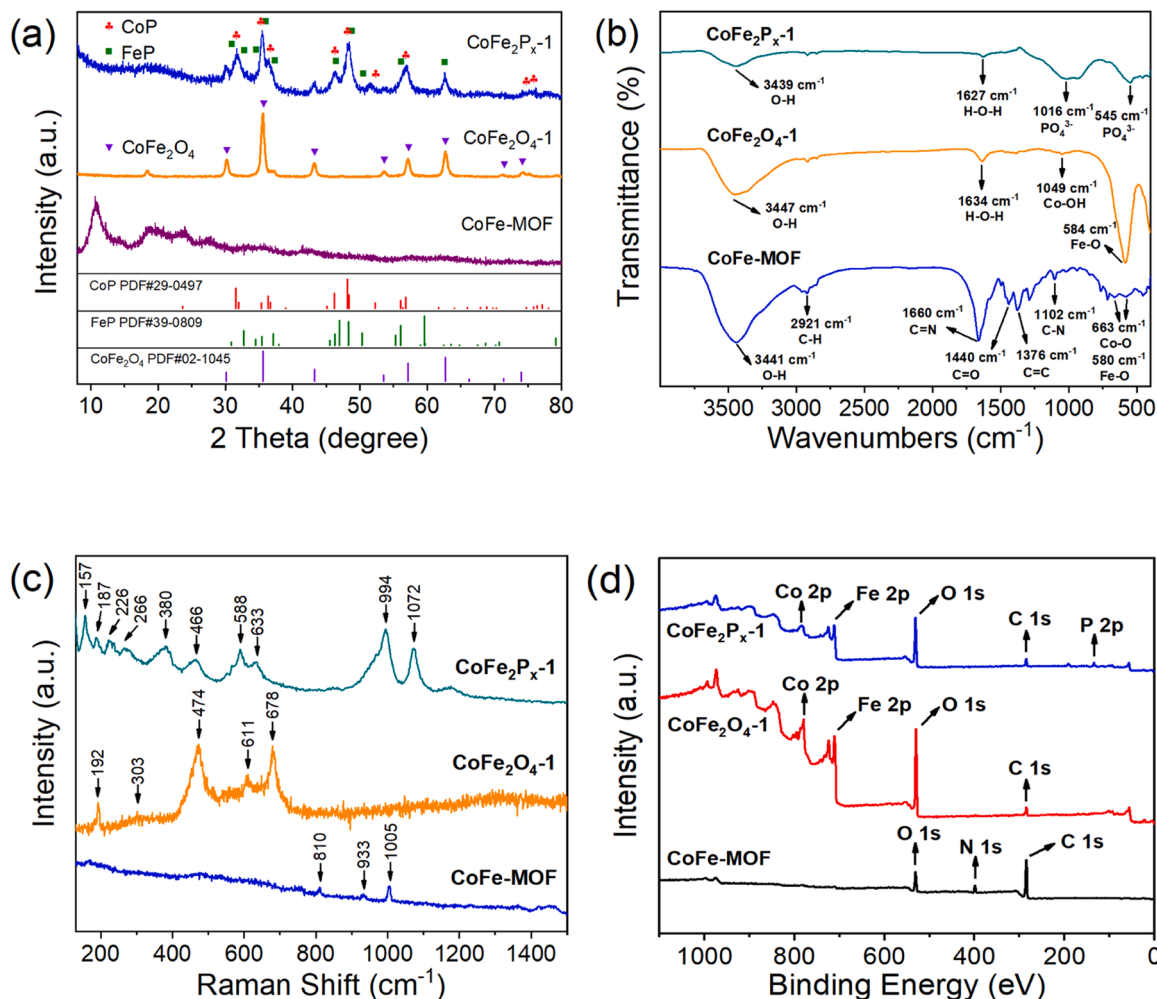


Fig. 1. XRD patterns (a), FT-IR (b), Raman (c), and XPS wide-scan (d) spectra of CoFe-MOF,  $\text{CoFe}_2\text{O}_4\text{-}1$ , and  $\text{CoFe}_2\text{P}_x\text{-}1$ .

781.2 eV and 796.2 eV and the second at 785.0 and 800.0 eV, with a binding energy gap of 15 eV, corresponded to Co 2p<sub>3/2</sub> and Co 2p<sub>1/2</sub>, respectively, confirming the co-existence of both Co(II) and Co(III) oxidation states [36]. Meanwhile, the Co 2p<sub>3/2</sub> at 778.2 eV and the Co 2p<sub>1/2</sub> at 793.2 eV were regarded as metallic state of Co, which was related to a characteristic bond of Co-P from cobalt-iron phosphide [26]. The Fe 2p spectrum (Fig. S2b) was composed of two spin-orbit doublets with the spin-energy separation of approximate 13 eV, and the deconvoluted Fe 2p<sub>3/2</sub> spectrum displayed two peaks located at 710.1 and 712.1 eV, which were assigned to Fe(II) and Fe(III), respectively. A high proportion (68.2%) of Fe(II) was detected in fresh catalyst, which was conducive to PMS activation. With regard to the P 2p spectrum (Fig. S2c), the doublets at 130.3/131.1 eV can be assigned to P 2p<sub>3/2</sub> and P 2p<sub>1/2</sub> in the form of phosphide, while another peak at 134.3 eV was attributed to the presence of oxidized phosphorous [26], which agreed with the result of FT-IR. Besides, the O 1s spectrum (Fig. S2d) was resolved into three individual peaks at 529.9, 531.2, and 532.4 eV, corresponding to the lattice oxygen (O<sub>L</sub>), oxygen vacancies (O<sub>V</sub>), and surface hydroxyl groups (O<sub>H</sub>), respectively.

### 3.2. Degradation of SCP in the presence of catalysts and oxidants

The degradation experiments were conducted under the condition of a low-speed mechanical oscillator rather than the high-speed magnetic stirring, which is much closer to the actual situation during practical application. The SCP removal efficiencies in various systems were

shown in Fig. 2a. Consistent with its small specific surface area (12.06 m<sup>2</sup> g<sup>-1</sup>, Fig. S3), nearly no SCP was adsorbed by CoFe<sub>2</sub>P<sub>x</sub>-1, suggesting the insignificant contribution of adsorption. Similarly, less than 12% of SCP was removed by PMS alone with zero order kinetics, which was attributed to the PMS direct oxidation via a nonradical oxidation pathway. Remarkably, 94.2% removal of SCP can be achieved within 30 min in the presence of both CoFe<sub>2</sub>P<sub>x</sub>-1 and PMS, indicating that PMS was activated by CoFe<sub>2</sub>P<sub>x</sub>-1. The degradation kinetic was fitted with the pseudo-first-order model, and the apparent rate constant (*k*) was calculated to be 0.090 min<sup>-1</sup> (Fig. S4). Compared with previous studies, the CoFe<sub>2</sub>P<sub>x</sub>-1/PMS system exhibited the highest SCP degradation rate constant (Table S2). The catalytic activities of CoFe<sub>2</sub>P<sub>x</sub> and its CoFe<sub>2</sub>O<sub>4</sub> precursor were compared. CoFe<sub>2</sub>O<sub>4</sub>-1, CoFe<sub>2</sub>O<sub>4</sub>-2, and CoFe<sub>2</sub>O<sub>4</sub>-3 were the precursors synthesized at 450, 650 and 850 °C, respectively, and the phosphides prepared from the corresponding CoFe<sub>2</sub>O<sub>4</sub> precursors were labelled as CoFe<sub>2</sub>P<sub>x</sub>-1, CoFe<sub>2</sub>P<sub>x</sub>-2, and CoFe<sub>2</sub>P<sub>x</sub>-3. As shown in Fig. 2b, the catalytic performance of oxides and phosphides was both negatively correlated with the synthesis temperature. However, the catalytic activity of CoFe<sub>2</sub>P<sub>x</sub> to degrade SCP was similar to or better than the corresponding CoFe<sub>2</sub>O<sub>4</sub> precursor, indicating that phosphorization promoted the performance of catalysts to activate PMS.

Fig. 2c displayed that FeP exhibited inferior catalytic performance in PMS activation for SCP degradation. When CoFe-MOF or CoP was introduced, SCP concentration rapidly decreased, and almost complete removal was achieved within 10 min, which was consistent with the

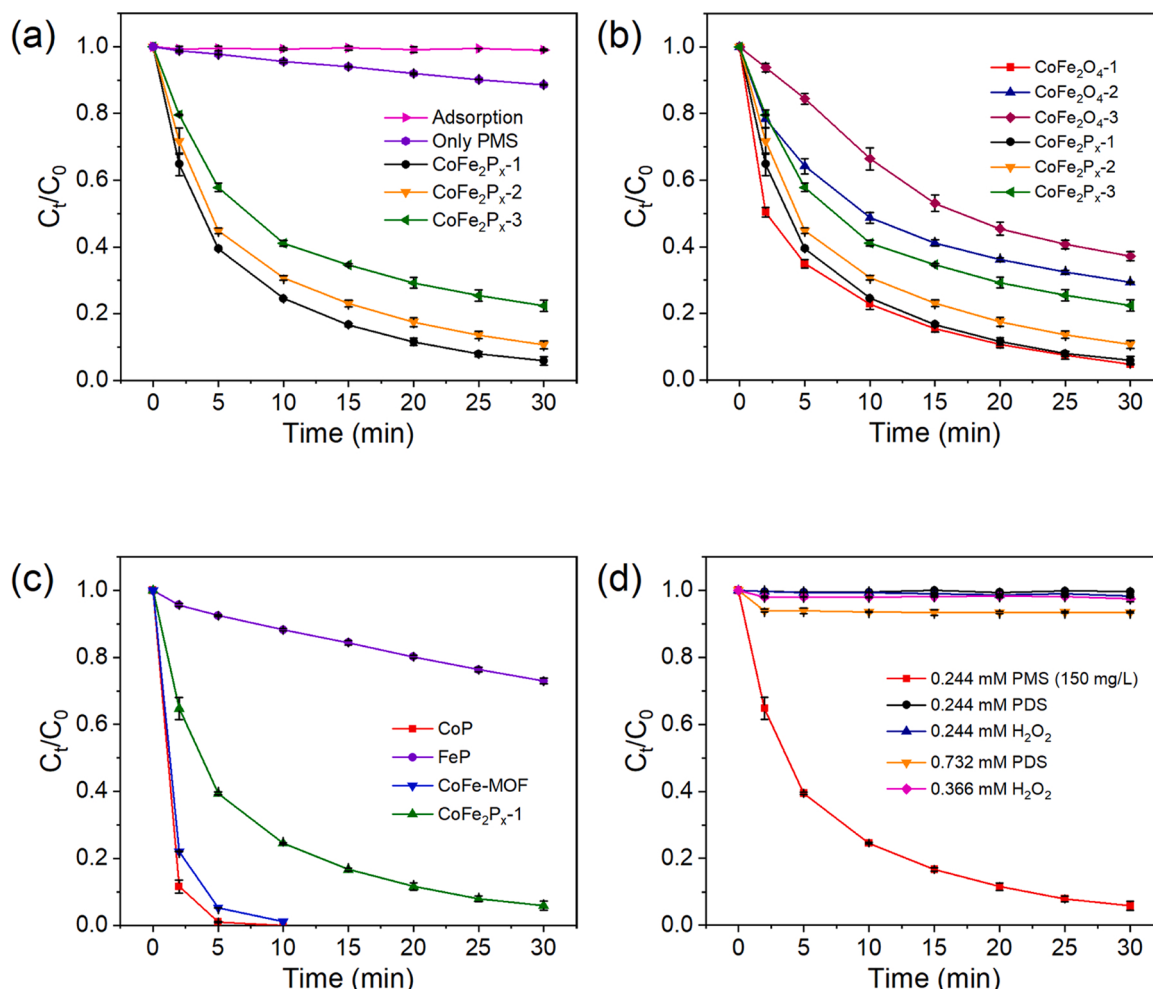


**Fig. 2.** Removal of SCP in the presence of CoFe<sub>2</sub>P<sub>x</sub>-based catalysts (a), CoFe<sub>2</sub>O<sub>4</sub>-based catalysts (b), CoFe-MOF precursor and mono-metallic phosphide catalysts (c) in PMS system, and the effects of various oxidants activated by CoFe<sub>2</sub>P<sub>x</sub>-1 on the SCP removal (d). Conditions: [Catalyst] = 0.1 g L<sup>-1</sup>, [SCP] = 10 mg L<sup>-1</sup>, [PMS] = 150 mg L<sup>-1</sup>, initial pH = 6.9. The dosage of different oxidants was calculated based on the molar concentration (for d).

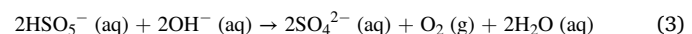
strong catalytic performance of previously reported  $\text{Co}_3(\text{BTC})_2$  [37] and  $\text{CoP}$  [38]. However, 3.31 and 4.70  $\text{mg L}^{-1}$  of leached Co were detected in  $\text{CoFe-MOF}/\text{PMS}$  and  $\text{CoP}/\text{PMS}$  systems, respectively, far exceeding the permissible discharge limit ( $1.0 \text{ mg L}^{-1}$ ) for industrial wastes according to the Chinese National Standard (GB 25467–2010). The extremely high amount of Co leaching limited their practical application. Meanwhile, the leached Co concentration in  $\text{CoFe}_2\text{O}_4\text{-1}/\text{PMS}$  system was  $0.21 \text{ mg L}^{-1}$ , similar to the levels reported in previous studies [39]. The leached concentration of cobalt ions after 30 min's reaction was only  $0.082 \text{ mg L}^{-1}$  in the  $\text{CoFe}_2\text{P}_{\text{x}}\text{-1}/\text{PMS}$  system, significantly lower than those of the previously reported cobalt-containing catalysts (Table S3) and the maximum allowable cobalt concentration in drinking and natural water ( $100 \mu\text{g L}^{-1}$ ) [40]. In addition, Fe leaching amount was as low as  $0.006 \text{ mg L}^{-1}$ . Therefore, phosphorization can effectively suppress the metal ion leaching and increase the stability of the catalyst.

The catalytic performance of  $\text{CoFe}_2\text{P}_{\text{x}}\text{-1}$  for different oxidants was further investigated. As shown in Fig. 2d, efficient degradation of SCP was achieved in  $\text{CoFe}_2\text{P}_{\text{x}}\text{-1}/\text{PMS}$  system, while almost no SCP removal was observed when PDS or  $\text{H}_2\text{O}_2$  was used as the oxidant. In practical applications, the unit price of PMS ( $2.2 \text{ USD kg}^{-1}$ ) is 3 and 1.5 times that of PDS ( $0.74 \text{ USD kg}^{-1}$ ) and  $\text{H}_2\text{O}_2$  ( $1.5 \text{ USD kg}^{-1}$ ), respectively [41]. However, even if the PDS or  $\text{H}_2\text{O}_2$  dosage corresponding to the price multiples was used, SCP was still hardly removed. This indicated that  $\text{CoFe}_2\text{P}_{\text{x}}\text{-1}$  was exclusively effective for PMS activation.

### 3.3. Influence of operating parameters on oxidation reactions

To better optimize the SCP removal by  $\text{CoFe}_2\text{P}_{\text{x}}\text{-1}/\text{PMS}$  system, influential factors were further examined, including pH, PMS concentration, and catalyst dosage.

As shown in Fig. 3a,  $\text{CoFe}_2\text{P}_{\text{x}}\text{-1}/\text{PMS}$  exhibited excellent SCP degradation performance within the initial pH ( $\text{pH}_0$ ) range of  $5.0 - 9.0$ . The pH values of the solution gradually decreased to around 4.0 and then remained stable (Fig. S5), which may be responsible for the almost consistent removal rate of SCP. A slight enhancement of SCP degradation rate was observed at the  $\text{pH}_0$  of 9.0, which may be due to the base activation of PMS [42]. However, when the pH of the solution was not adjusted ( $\text{pH}_0 = 3.6$ ) or the initial pH was 3.0 and 11.0, the pH values during the reaction remained stable and the SCP degradation was significantly inhibited. According to the  $\text{pK}_a$  values of PMS ( $\text{pK}_{\text{a}1} < 0$ ,  $\text{pK}_{\text{a}2} = 9.4$ ),  $\text{HSO}_5^-$  was the major PMS specie in strongly acidic solution. The stabilization effect of  $\text{H}^+$  on  $\text{HSO}_5^-$  hindered the interaction between  $\text{HSO}_5^-$  and the catalyst surface [43]. When the solution was under strongly alkaline condition,  $\text{HSO}_5^-$  would react with high concentration of  $\text{OH}^-$  and decompose to  $\text{SO}_4^{2-}$  and  $\text{O}_2$  (Eq. 3), which was responsible for the poor removal rate of SCP.



The SCP removal rate showed a positive dependence on PMS concentration (Fig. 3b), which was attributed to the generation of more ROS with the increasing amount of PMS. As the PMS concentration continued

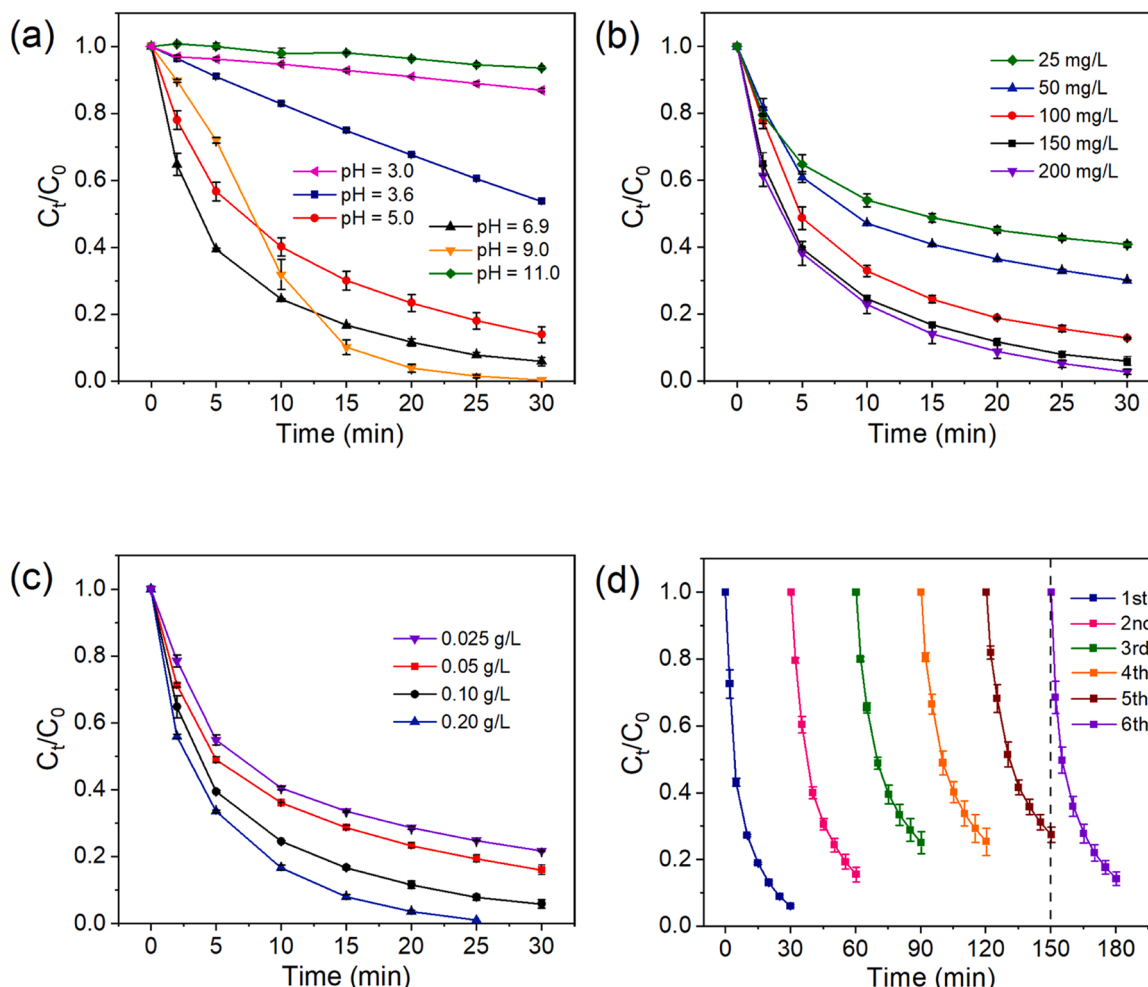
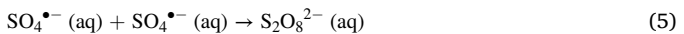
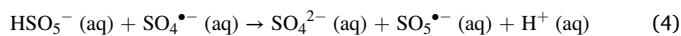


**Fig. 3.** Removal of SCP at different pH values (a), PMS dosages (b), and catalyst dosages (c), and reusability of  $\text{CoFe}_2\text{P}_{\text{x}}\text{-1}$  in  $\text{CoFe}_2\text{P}_{\text{x}}\text{-1}/\text{PMS}$  system for SCP removal (d). Conditions:  $[\text{CoFe}_2\text{P}_{\text{x}}\text{-1}] = 0.1 \text{ g L}^{-1}$ ,  $[\text{SCP}] = 10 \text{ mg L}^{-1}$ ,  $[\text{PMS}] = 150 \text{ mg L}^{-1}$ , initial pH = 6.9.

to increase, the removal rate first increased rapidly and then rose slightly, while only an increase of 3.2% was achieved when the PMS amount went up from 150 to 200 mg L<sup>-1</sup>. The potential reason is that overdosed PMS with insufficient catalyst may scavenge ROS (Eq. 4). Besides, self-scavenging of the excessive ROS in solution also inhibits SCP oxidation (Eq. 5).



An increase in catalyst dosage within the tested range exhibited a significant positive effect on SCP degradation (Fig. 3c). When the CoFe<sub>2</sub>P<sub>x</sub>-1 dosage was increased to 0.2 g L<sup>-1</sup>, complete degradation of SCP was achieved within 25 min. Obviously, with the increase of catalyst dosage, more reaction sites on catalyst surface would participate in PMS activation, which is conducive to the generation of ROS.

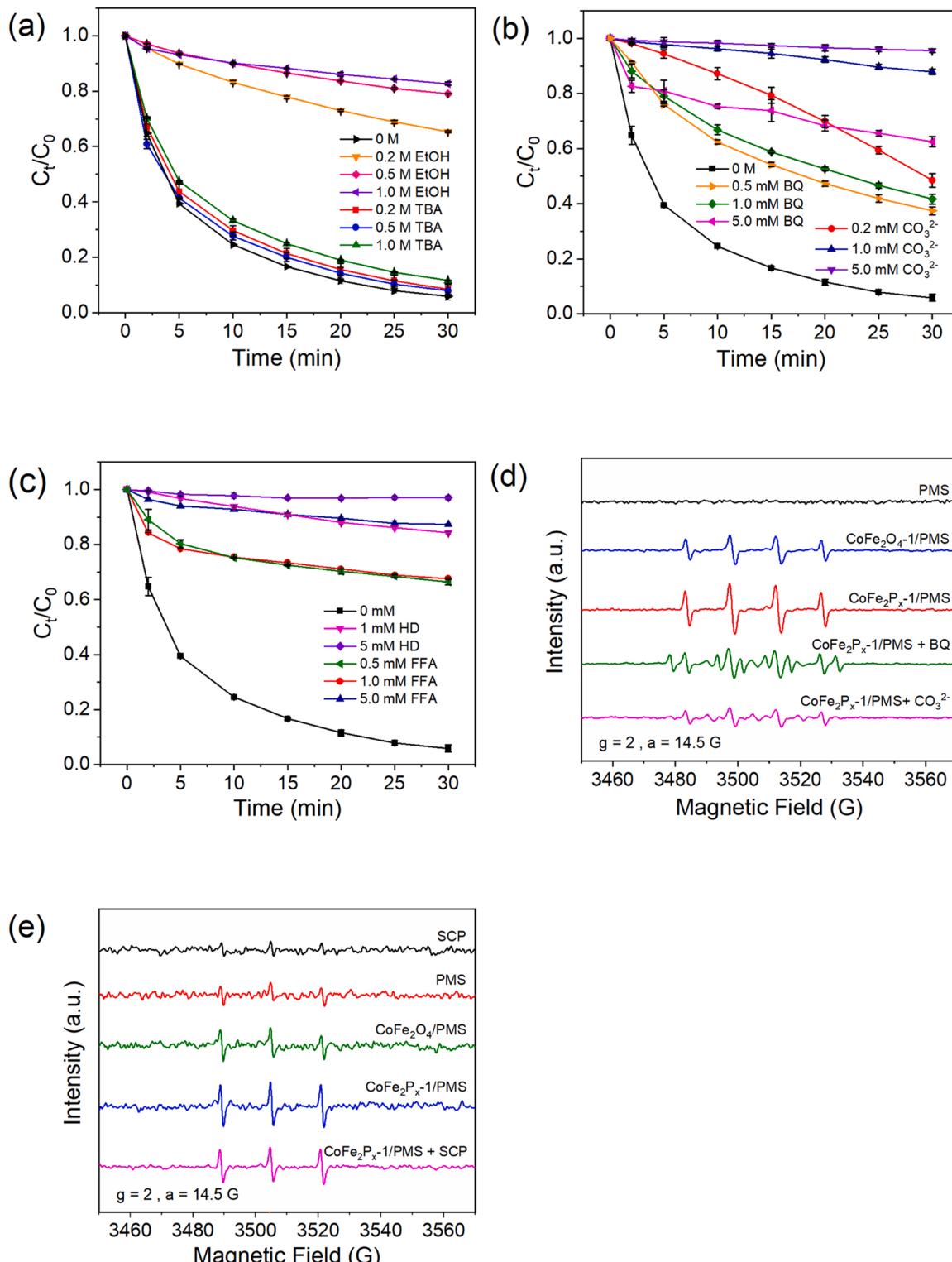


**Fig. 4.** Effect of different kinds of scavengers on SCP removal in CoFe<sub>2</sub>P<sub>x</sub>-1/PMS system (a, b, and c), and DMPO (d) and TEMP trapped (e) EPR spectra in various systems. Conditions: [CoFe<sub>2</sub>P<sub>x</sub>-1] = 0.1 g L<sup>-1</sup>, [SCP] = 10 mg L<sup>-1</sup>, [PMS] = 150 mg L<sup>-1</sup>, initial pH = 6.9. The reaction time was 5 min for d and e.

### 3.4. Reusability and regeneration of catalyst

The stability and reusability of CoFe<sub>2</sub>P<sub>x</sub>-1 in catalytic PMS system were evaluated by five consecutive experiments. As shown in Fig. 3d, the SCP removal efficiencies slightly decreased during the cyclic reactions, which might be attributed to the adsorption of degradation intermediates that prevented the interactions among PMS, SCP and the catalyst. Once the adsorption was saturated, the SCP removal efficiency was stable. Furthermore, the catalytic performance of CoFe<sub>2</sub>P<sub>x</sub>-1 was fully recovered after a thermal treatment at 350 °C for 2 h in an Ar atmosphere, due to the removal of the adsorbed intermediates during calcination.

CoFe<sub>2</sub>P<sub>x</sub>-1 has a saturation magnetization of 3.6 emu g<sup>-1</sup>, whereas the CoFe<sub>2</sub>O<sub>4</sub> precursor shows a high magnetization of 62.3 emu g<sup>-1</sup> (Fig. S6). Similar results have also been reported that phosphorization caused a decrease in magnetic properties [44]. The inset of Fig. S6 shows that CoFe<sub>2</sub>P<sub>x</sub>-1 could be separated easily from the solution by an external magnet, suggesting the convenience for its reusability. Moreover, the weak magnetic property of CoFe<sub>2</sub>P<sub>x</sub>-1 reduced the aggregation between the catalyst particles, which is in favor of the catalytic performance.

The leached Co ions in five cycles were 0.082, 0.053, 0.027, 0.024, and 0.023 mg L<sup>-1</sup>, respectively, which gradually decreased and tended to be stable. The leaching amount of Fe ions was 0.006, 0.003 and 0.001 mg L<sup>-1</sup> in the first three cycles, respectively, and undetectable in the subsequent cycles. These results demonstrated the excellent stability and recyclability of CoFe<sub>2</sub>P<sub>x</sub>-1 for potential applications.

### 3.5. Identification of radicals and their quantitative contributions

#### 3.5.1. Quenching experiments

Quenching experiments were conducted to identify the reactive species in CoFe<sub>2</sub>P<sub>x</sub>-1/PMS system. To achieve complete scavenging, scavengers of gradient concentrations were employed.

Ethanol (EtOH) with α-H is considered as an excellent scavenger for both SO<sub>4</sub><sup>•-</sup> ( $k = 1.6\text{--}7.7 \times 10^7 \text{ M}^{-1} \text{ s}^{-1}$ ) and •OH ( $k = 1.9 \times 10^9 \text{ M}^{-1} \text{ s}^{-1}$ ), whereas TBA without α-H is clearly more effective for •OH ( $k = 3.8\text{--}7.6 \times 10^8 \text{ M}^{-1} \text{ s}^{-1}$ ) than for SO<sub>4</sub><sup>•-</sup> ( $k = 4.0\text{--}8.1 \times 10^5 \text{ M}^{-1} \text{ s}^{-1}$ ) [1,2]. The introduction of 1 M TBA weakly inhibited the SCP removal, while the presence of 1 M EtOH significantly depressed the removal rate from 94.2% to 17.3% in 30 min (Fig. 4a), implying that •OH played a minor role and SO<sub>4</sub><sup>•-</sup> was the dominant radical in SCP elimination.

The role of O<sub>2</sub><sup>•-</sup> was investigated by adding corresponding scavengers. *Para*-benzoquinone (BQ) has been widely used as the scavenger of O<sub>2</sub><sup>•-</sup> ( $k = 2.9 \times 10^9 \text{ M}^{-1} \text{ s}^{-1}$ ) [45]. The introduction of 1 mM BQ showed remarkable inhibition effect on SCP removal (Fig. 4b), suggesting that O<sub>2</sub><sup>•-</sup> participated in the catalytic degradation. However, BQ could also react with SO<sub>4</sub><sup>•-</sup> at relatively high rate constant (Table S4). Thus, another selective scavenger, CO<sub>3</sub><sup>2-</sup>, was used to further confirm the generation and role of O<sub>2</sub><sup>•-</sup>. CO<sub>3</sub><sup>2-</sup> manifested a relatively high second order rate with O<sub>2</sub><sup>•-</sup> ( $k = 5 \times 10^8 \text{ M}^{-1} \text{ s}^{-1}$ ) and •OH ( $k = 4 \times 10^8 \text{ M}^{-1} \text{ s}^{-1}$ ), whereas a poor reactivity with SO<sub>4</sub><sup>•-</sup> ( $k = 6.1 \times 10^6 \text{ M}^{-1} \text{ s}^{-1}$ ). As shown in Fig. 4b, addition of CO<sub>3</sub><sup>2-</sup> significantly inhibited the degradation efficiency of SCP. In presence of 0.2 mM CO<sub>3</sub><sup>2-</sup>, the removal rate decreased to 51.5%, and the SCP degradation almost completely stopped when CO<sub>3</sub><sup>2-</sup> concentration reached 1 mM. As discussed above, •OH contributed a minor proportion in CoFe<sub>2</sub>P<sub>x</sub>-1/PMS system. Moreover, the first-order rate constant of 1 M TBA with SO<sub>4</sub><sup>•-</sup> ( $k = 4.0\text{--}8.1 \times 10^5 \text{ s}^{-1}$ ) was 2 orders of magnitude higher than that of 1 mM CO<sub>3</sub><sup>2-</sup> ( $k = 6.1 \times 10^3 \text{ s}^{-1}$ ), but the inhibition effect by 1 M TBA was slight, suggesting the quenching effect of 1 mM CO<sub>3</sub><sup>2-</sup> on SO<sub>4</sub><sup>•-</sup> was also negligible. Therefore, O<sub>2</sub><sup>•-</sup> was generated and played an important role in the catalytic degradation.

The role of O<sub>2</sub> was also evaluated. As common scavengers for O<sub>2</sub>, L-histidine (HD) and azide sodium (NaN<sub>3</sub>) have been questioned for their possible reaction with PMS, and the decrement of oxidation

performance may be due to the PMS depletion [46]. In presence of 1 mM HD, the SCP degradation was almost suspended, with only 15.8% removal in 30 min (Fig. 4c). On the contrary, the direct reaction between furfuryl alcohol (FFA) and PMS was negligible [47]. As shown in Fig. 4c, 1 mM of FFA exhibited a noticeable suppression of SCP removal from 94.2% to 32.4%, indicating that O<sub>2</sub> contributed to SCP elimination. However, the reaction rate constant between FFA and SO<sub>4</sub><sup>•-</sup> was not available (Table S4), i.e. FFA may also react with SO<sub>4</sub><sup>•-</sup> and the role of O<sub>2</sub> may be overestimated. Therefore, EPR analyses were conducted to further confirm the above results.

#### 3.5.2. EPR analyses

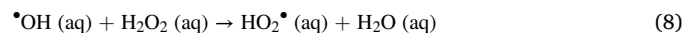
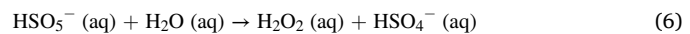
As shown in Fig. 4d, no characteristic peaks were observed in DMPO or PMS alone system. After CoFe<sub>2</sub>P<sub>x</sub>-1 addition, intense signals of •OH (DMPO-•OH adducts, with hyperfine couplings  $\alpha(\text{N}) = \alpha(\text{H}) = 14.9 \text{ G}$ ) were detected, much higher than those of SO<sub>4</sub><sup>•-</sup> (DMPO-SO<sub>4</sub><sup>•-</sup> adducts, with hyperfine splitting constants of  $\alpha(\text{N}) = 13.2 \text{ G}$ ,  $\alpha(\text{H}) = 9.6 \text{ G}$ ,  $\alpha(\text{H}) = 1.48 \text{ G}$ ,  $\alpha(\text{H}) = 0.78 \text{ G}$ ). This result, inconsistent with quenching experiments, is due to the fast transformation of DMPO-SO<sub>4</sub><sup>•-</sup> to DMPO-•OH [48,49].

Fig. 4e shows the weak characteristic 1:1:1 triplet signal for TEMP-O<sub>2</sub><sup>•-</sup> adducts in the cases of sole SCP or PMS system, which was due to the fact that TEMP, from which one electron was abstracted, could react with dissolved oxygen and result in misleading signals of TEMP-O<sub>2</sub><sup>•-</sup> adducts [50]. Notably, much stronger signals of TEMP-O<sub>2</sub><sup>•-</sup> were detected in CoFe<sub>2</sub>P<sub>x</sub>-1/PMS system, suggesting that O<sub>2</sub> was generated. The addition of SCP decreased the intensity of TEMP-O<sub>2</sub><sup>•-</sup> signals, which agreed with the speculation that O<sub>2</sub> contributed to SCP removal.

### 3.6. Mechanism of PMS activation

To better comprehend the role of CoFe<sub>2</sub>P<sub>x</sub>-1 in PMS activation, the elemental proportions and chemical states of the catalyst were investigated by analyzing the XPS spectra of CoFe<sub>2</sub>P<sub>x</sub>-1 before and after the catalytic experiment (Fig. S2a-d). The binding energy of the prominent peaks of Co 2p and Fe 2p shifted slightly after the activation reaction, indicating the changes of elemental valence. The ratio of Co(II)/Co(III) decreased from 0.58 in virgin CoFe<sub>2</sub>P<sub>x</sub>-1 to 0.48 in used catalyst, suggesting that Co(II) donated electrons to PMS during the activation. The ratio of Fe(III)/Fe(II) increased from 0.47 to 0.62 after the catalytic reaction, implying the oxidization of some Fe(II) to Fe(III). After the reaction, the relative intensity of O<sub>L</sub> reduced from 47.5% to 29.2%, while the O<sub>V</sub> and O<sub>H</sub> increased from 48.0% to 59.0% and from 4.5% to 11.8%, respectively, indicating that these oxygen species contributed to the PMS activation.

Several views have been proposed regarding the origin of O<sub>2</sub><sup>•-</sup> during PMS activation. For example, during the reaction of PMS and H<sub>2</sub>O, the generated H<sub>2</sub>O<sub>2</sub> could be further converted into O<sub>2</sub><sup>•-</sup> (Eqs. 6–9) [51]. However, as shown in Fig. 5a, the addition of H<sub>2</sub>O<sub>2</sub> in CoFe<sub>2</sub>P<sub>x</sub>-1/PMS system had little effect on SCP removal, implying that the formed H<sub>2</sub>O<sub>2</sub> may play a minor role in the generation of O<sub>2</sub><sup>•-</sup>. Some researchers believed that O<sub>2</sub><sup>•-</sup> could be generated by the transfer of the abundant localized electrons of O<sub>V</sub> to dissolved oxygen (DO) (Eq. 10) [52]. Insignificant variation of SCP removal was observed after N<sub>2</sub> bubbling in our study (Fig. 5a), revealing that DO should be produced by the decomposition of PMS (Eq. 11) [53]. Moreover, O<sub>2</sub> could be generated through the release of electrons from O<sub>L</sub>, accompanied with the formation of new O<sub>V</sub> [47,53]. O<sub>2</sub><sup>•-</sup> could also be directly formed through the reaction between O<sub>V</sub> and PMS (Eq. 12) [54,55].



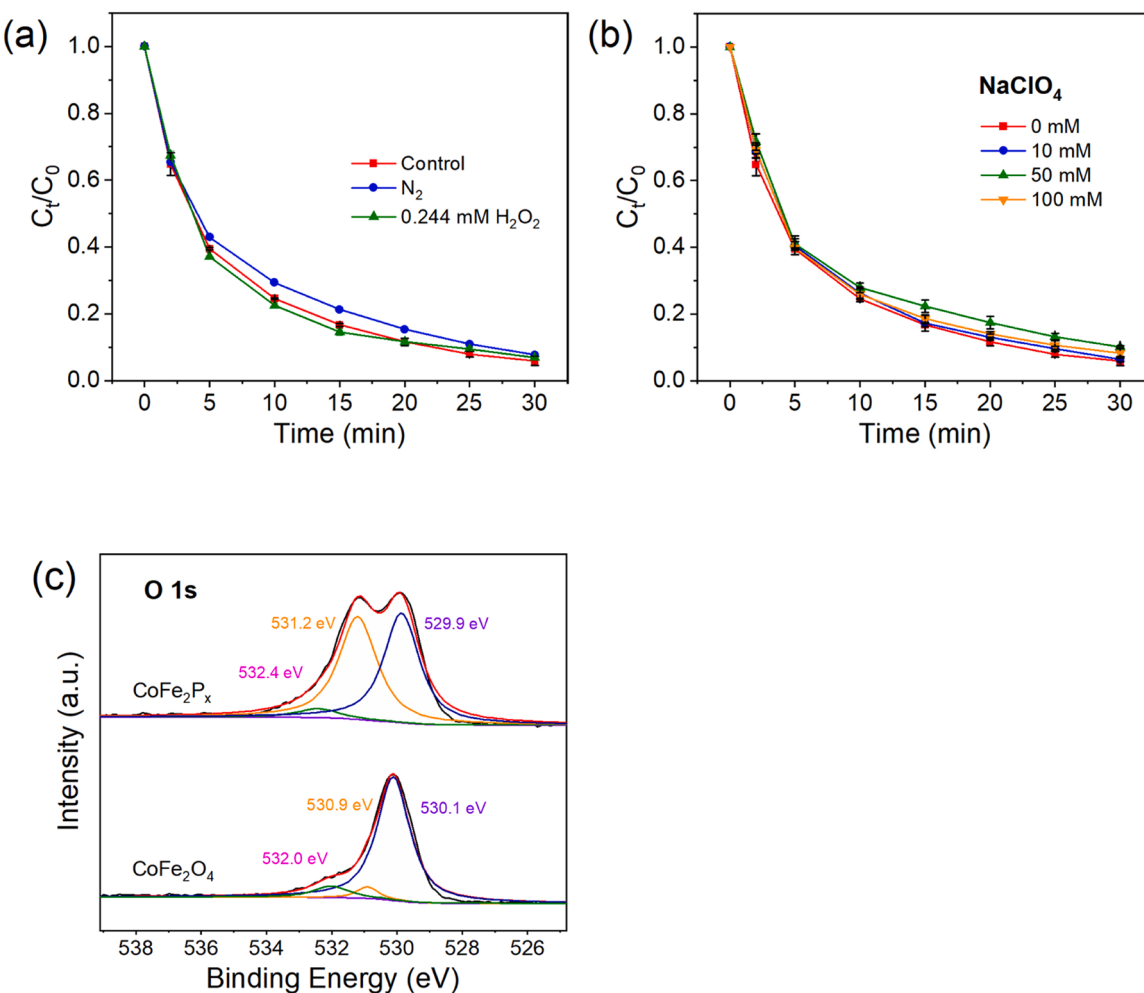
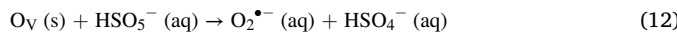
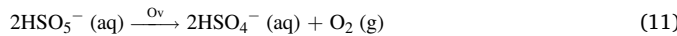
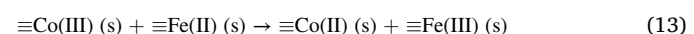


**Fig. 5.** Effect of N<sub>2</sub> bubbling, H<sub>2</sub>O<sub>2</sub> (a) and NaClO<sub>4</sub> (b) on SCP removal in CoFe<sub>2</sub>P<sub>x</sub>-1/PMS system, and high resolution of O 1s XPS spectra of fresh CoFe<sub>2</sub>P<sub>x</sub>-1 and CoFe<sub>2</sub>O<sub>4</sub>-1 (c). Conditions: [CoFe<sub>2</sub>P<sub>x</sub>-1] = 0.1 g L<sup>-1</sup>, [SCP] = 10 mg L<sup>-1</sup>, [PMS] = 150 mg L<sup>-1</sup>, initial pH = 6.9.



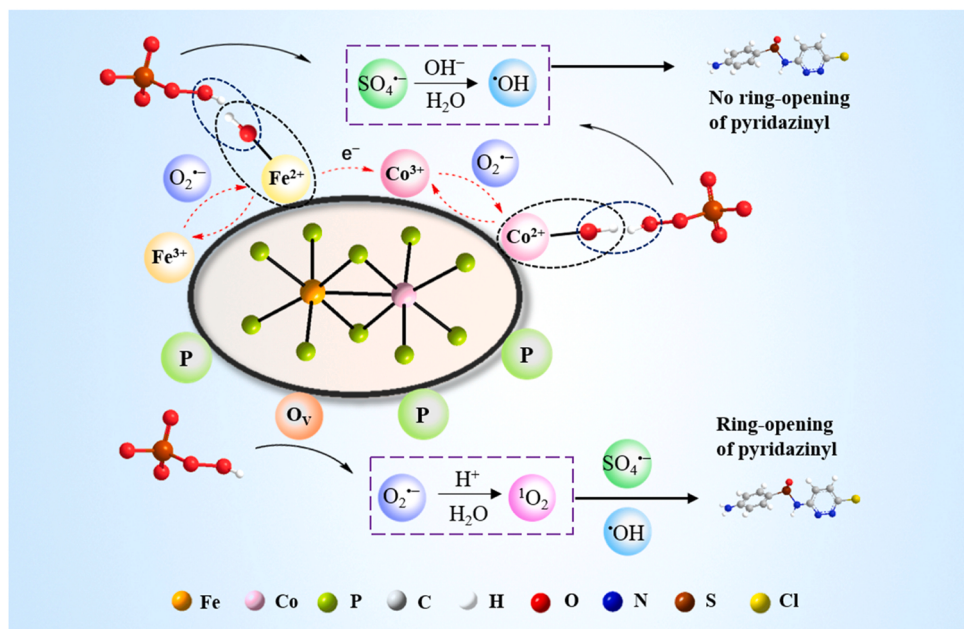
The redox cycle of Co(III)/Co(II) and Fe(III)/Fe(II) played a vital role in PMS activation. Previous studies suggested that Co(III) and Fe(III) were reduced by the reaction with PMS [10,11]. Meanwhile, Co(III) could also be reduced by electron transfer from Fe(II) (Eq. 13), which was considered to be the synergistic effect of the two metals in PMS activation [10,11]. However, the standard redox potentials of Fe(III)/Fe(II) and HSO<sub>5</sub><sup>-</sup>/SO<sub>5</sub><sup>2-</sup> are 0.77 and 1.1 V, respectively, implying that the reaction between Fe(III) and HSO<sub>5</sub><sup>-</sup> to regenerate Fe(II) was thermodynamically unfavorable. Considering that the standard redox potential of O<sub>2</sub><sup>•-</sup>/O<sub>2</sub> is -0.33 V [2], we speculated that O<sub>2</sub><sup>•-</sup> generated on the surface of CoFe<sub>2</sub>P<sub>x</sub>-1 contributed to the regeneration of Fe(II) and Co(II) and further facilitated the production of SO<sub>4</sub><sup>2-</sup>. To verify the potential of O<sub>2</sub><sup>•-</sup> in contributing to the generation of SO<sub>4</sub><sup>2-</sup>, BQ and CO<sub>3</sub><sup>2-</sup> were added in EPR tests. As shown in Fig. 4d, when 0.5 mM BQ or CO<sub>3</sub><sup>2-</sup> was introduced in CoFe<sub>2</sub>P<sub>x</sub>-1/PMS system, the signal intensity of DMPO<sup>•-</sup>OH adducts was significantly weakened. Besides, comparing the time-dependent signal changes of DMPO<sup>•-</sup>OH and TEMP<sup>-1</sup>O<sub>2</sub>, a similar trend was observed (Fig. S7). The intensity of these signals first

decreased then increased, which is consistent with the role of O<sub>2</sub><sup>•-</sup> in facilitating the production of SO<sub>4</sub><sup>2-</sup> and <sup>1</sup>O<sub>2</sub> (discussed later in this section).



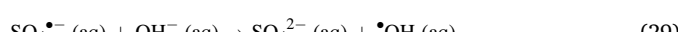
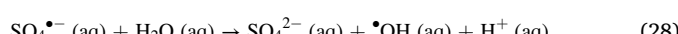
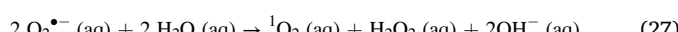
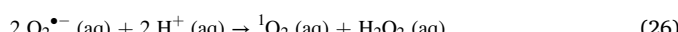
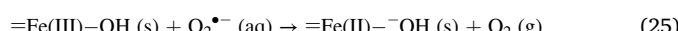
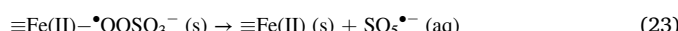
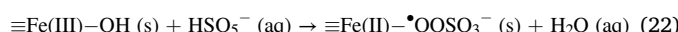
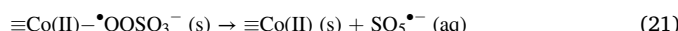
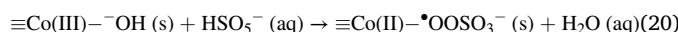
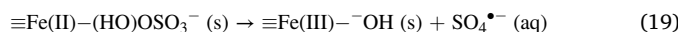
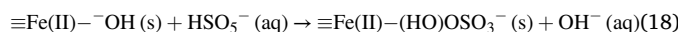
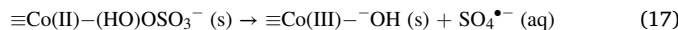
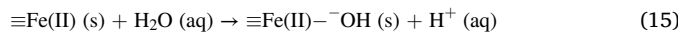
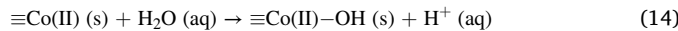
When the ionic strength in a heterogeneous system increased, outer-sphere interactions (electrostatic bonding) would be suppressed due to the compression of the electric double layers, while inner-sphere complexation (ionic bonding or covalent bonding) was not affected [43]. Due to its inertness to powerful radicals, NaClO<sub>4</sub> was employed to adjust the ionic strength in the reaction solution. Fig. 5b shows that SCP removal was barely influenced in presence of NaClO<sub>4</sub> from 10 to 100 mM, indicating that the interactions between HSO<sub>5</sub><sup>-</sup> and the catalyst surface proceeded via ionic bonding.

Based on the above discussion, a possible mechanism of PMS activation by CoFe<sub>2</sub>P<sub>x</sub>-1 was proposed and schematically displayed in Scheme 1. Surface hydroxyl groups (Co(II)-OH and Fe(II)-OH) were generated by the dissociation of adsorbed water molecules (Eqs. 14 and 15). Then, HSO<sub>5</sub><sup>-</sup> reacted with the surface hydroxyl groups to form inner-sphere complex (Eqs. 16 and 18). After a one-electron transfer, SO<sub>4</sub><sup>2-</sup> was produced, accompanied with the increased valence state of the metals (Eqs. 17 and 19). In addition to the PMS-based reduction process (Eqs. 20-23), O<sub>2</sub><sup>•-</sup> played a critical role in the regeneration of low-valent metals (Eqs. 24 and 25). As a result, two complete redox cycles of Co(III)/Co(II) and Fe(III)/Fe(II) were achieved, which favored the continuous activation of PMS. Meanwhile, <sup>1</sup>O<sub>2</sub> and <sup>•</sup>OH were



**Scheme 1.** Schematic illustration of the proposed mechanism of PMS activation on the surface of catalyst.

produced by the reactions of  $O_2^{•-}$  with  $H_2O/H^+$  and  $SO_4^{•-}$  with  $H_2O/\cdot OH$ , respectively (Eqs. 26–29).



### 3.7. Comparison between oxides and phosphides and the role of P

As previously reported,  $SO_4^{•-}$  and  $\cdot OH$  were identified as the primary ROS in the  $CoFe_2O_4$ /PMS system [39,56]. Fig. 4e also displays that the signals of  $TEMP-^1O_2$  adducts in  $CoFe_2O_4$ -1/PMS system were not much different from those in the blank group. However,  $O_2^{•-}$  and  $^1O_2$  appeared in  $CoFe_2P_x$ -1/PMS system and played an important role in the degradation of target pollutant. This difference may be mainly due to the difference in surface oxygen composition of the two types of catalysts.

During the phosphorization process, the incorporation of P is accompanied with the formation of substantial oxygen vacancies. According to the deconvoluted O 1s spectra (Fig. 5c), the oxygen vacancy contents in  $CoFe_2O_4$ -1 and  $CoFe_2P_x$ -1 were 5.3% and 48.0%, respectively. The presence of oxygen vacancies in  $CoFe_2P_x$ -1 contributed to the generation of  $O_2^{•-}$  and  $^1O_2$  [54,55].

In addition, compared with  $CoFe_2O_4$ -1/PMS system, the concentration of leached Co ions was reduced by 61.0% in  $CoFe_2P_x$ -1/PMS system under the same reaction parameters, as mentioned in Section 3.2. Phosphorization process is in favor of the inhibition of Co ion leaching, which might be owing to two reasons. First, the distance between cobalt and iron atoms in  $CoFe_2O_4$  and  $CoFe_2P_x$  is 334.98 and 267.24 pm (Fig. 6a), respectively. The shorter interatomic distance means a more intimate Co-Fe interaction in the crystal lattice of  $CoFe_2P_x$ -1 [28,57], which can greatly suppress the metal ions leaching. Second, the atomic radius of phosphorus is much larger than that of oxygen. As shown in Fig. 6b, the metal atoms in  $CoFe_2O_4$  are mostly exposed, while the metal atoms in the phosphide are half-wrapped by the network formed by phosphorus, which is unfavorable to metal leaching.

### 3.8. Effects of anions and humic acid on SCP degradation

Inorganic anions and natural organic matter (NOM) are ubiquitous in real water bodies, and can affect the performance of AOPs in contaminants removal. Therefore, SCP degradation in  $CoFe_2P_x$ -1/PMS system was evaluated in the presence of common anions ( $Cl^-$ ,  $CO_3^{2-}$ ,  $HCO_3^-$ , and  $SO_4^{2-}$ ) and humic acid.

As shown in Fig. S8a, 1 mM of  $Cl^-$  exhibited a slight inhibitory effect on SCP removal. However, when  $Cl^-$  concentration was increased to 10 mM, the degradation efficiency was significantly accelerated with the reaction time decreased from 30 to 20 min. Previous studies reported that  $Cl^-$  could serve as sinks of  $SO_4^{•-}$  and react with  $HSO_5^-$  to generate various active chlorine species ( $Cl_2$ , 1.36 V;  $Cl^*$ , 2.4 V;  $Cl_2^{•-}$ , 2.1 V;  $CLOH^{•-}$ ;  $HOCl$ ) [58,59]. Among them,  $HOCl$  is a special one, which could cause instantaneous degradation of targeted pollutant [60]. The production of  $HOCl$  is proportional to the initial  $Cl^-$  dosage [61]. At the  $Cl^-$  concentration of 1 mM,  $Cl^-$  tended to react with  $SO_4^{•-}$  to form less reactive  $Cl$  species. With the increasing of  $Cl^-$  dosage from 5 to 10 mM, more  $HOCl$  species were generated and the degradation kinetics of SCP gradually increased. Therefore, the effect of  $Cl^-$  on SCP removal

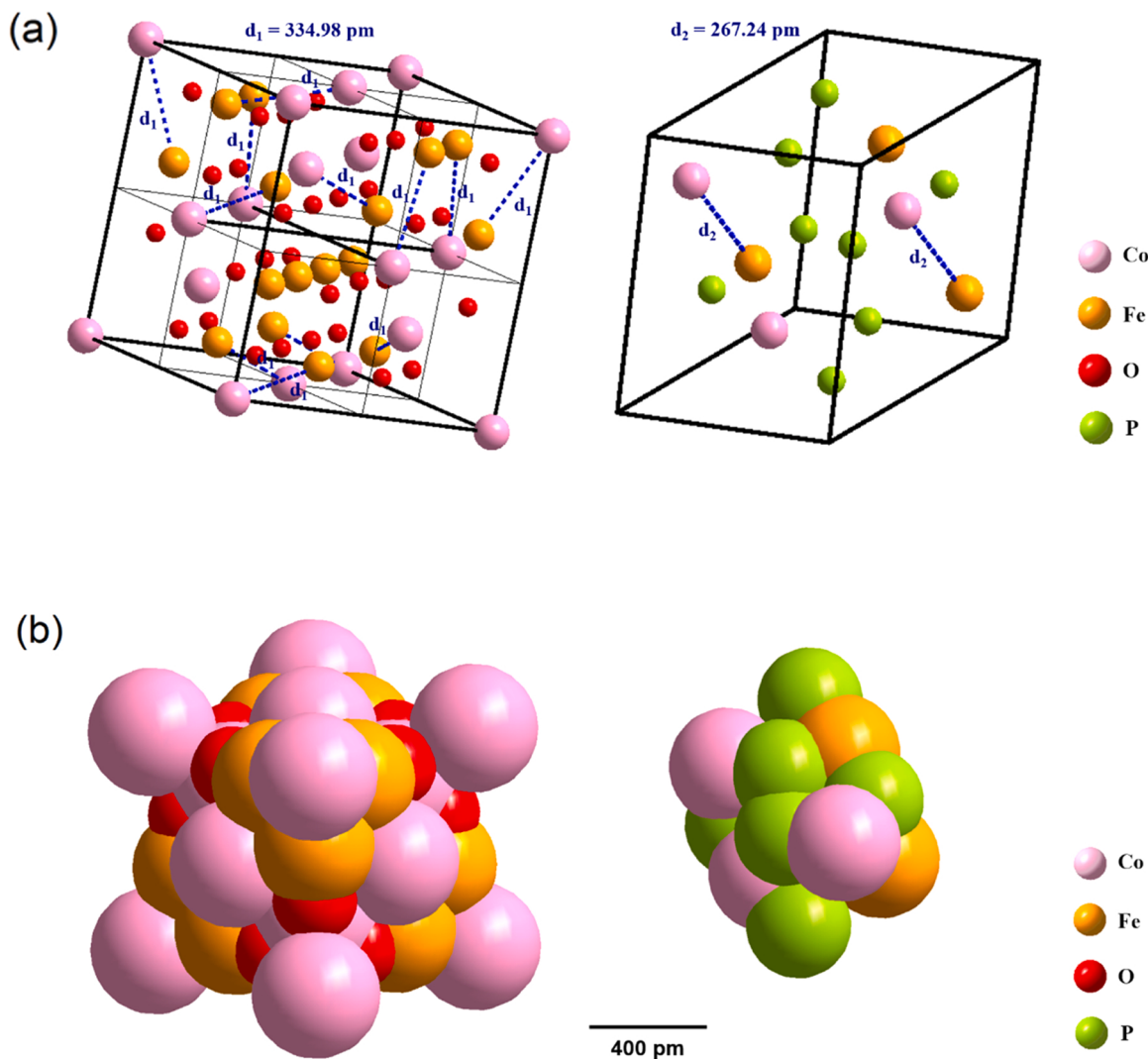


**Fig. 6.** The distance between cobalt and iron atoms in the crystal structure (a) and the space-filling model (b) of  $\text{CoFe}_2\text{O}_4$  and  $\text{CoFe}_2\text{P}_x$ .

is the result of the combined action between the primary ROS and the secondary less reactive chloride species. Despite the enhanced SCP removal efficiency, the presence of  $\text{Cl}^-$  may lead to the formation of some more toxic chlorinated transformation products. As depicted in Fig. S8b, the SCP degradation rate was sharply retarded when  $\text{HCO}_3^-$  was present. The inhibitory effect was mainly attributed to the consumption of reactive species ( $\text{SO}_4^{2-}$ ,  $\cdot\text{OH}$ , and  $\text{O}_2^{\bullet-}$ ) by  $\text{HCO}_3^-$  to form less active  $\text{HCO}_3^{\bullet}/\text{CO}_3^{2-}$ . In addition,  $\text{HCO}_3^-$  could form complex with the surface of metal-based catalyst and occupy its active sites. Therefore, the inhibitory effect of  $\text{HCO}_3^-$  gradually enhanced as its concentration increased from 1 to 10 mM. The addition of  $\text{SO}_4^{2-}$  with various concentrations exhibited slightly inhibitory effect on SCP removal (Fig. S8c) and the interference of  $\text{CO}_3^{2-}$  was as discussed above.

The existence of NOM usually causes apparent inhibitory effect on substrate degradation by quenching ROS or blocking active sites of catalyst. However, an excellent resistance of  $\text{CoFe}_2\text{P}_x$ -1/PMS system to NOM was observed. As shown in Fig. S8d, although the increased concentration of HA slightly inhibited the degradation of SCP, the degradation rate in  $\text{CoFe}_2\text{P}_x$ -1/PMS/HA system was still superior than that in the control sample (without HA). Similar results have been reported in the PMS activation by  $\text{Co}_9\text{S}_8$  [47] and  $\text{La}_2\text{CuO}_{4.8}$  [62]. Furthermore, the performance of  $\text{CoFe}_2\text{P}_x$ -1/PMS system was tested in tap water and surface water to evaluate the integrated effects of substrate ions and NOM on SCP removal. Specifically, the surface water was taken from

Dasha River ( $22.596797^\circ \text{N}, 113.979424^\circ \text{E}$ ) and used directly without treatment. As shown in Fig. S8e, 92.8% and 78.5% of SCP were degraded in tap water and surface water, respectively, further revealing the promising potential of  $\text{CoFe}_2\text{P}_x$ -1/PMS system in practical wastewater treatment.

### 3.9. SCP degradation pathways

The transformation products of SCP in  $\text{CoFe}_2\text{P}_x$ -1/PMS system were identified by full scan on UHPLC-MS/MS and product ion scan on UHPLC-Q-Orbitrap HRMS. A total of 21 intermediates were detected and the proposed oxidation pathways are illustrated in Fig. 7, with the corresponding structures and other details provided in Fig. S9.

In pathway I, the ion of  $m/z$  300.7 with an -NHOH group was deemed as the hydroxylation product of the aniline ring. Then  $m/z$  330.7 was generated via nitrification and hydroxylation by the attack of  $\text{SO}_4^{\bullet-}$ , followed with the formation of  $m/z$  305.3 through the ring-opening of pyridazinyl induced by  ${}^1\text{O}_2$ . Meanwhile,  $m/z$  312.3 was formed by dechlorination of  $m/z$  330.7 under the action of  $\cdot\text{OH}$ .

Pathway II was initiated with the Smiles-type rearrangement reaction followed by  $\text{SO}_2$  extrusion to produce  $m/z$  220.7. After the nitration and hydroxylation of the product, the ring-opening of pyridazinyl occurred, resulting in the generation of  $m/z$  225.3 and  $m/z$  273.3. With the progress of the reaction, the cleavage of C-N bond via an electron-

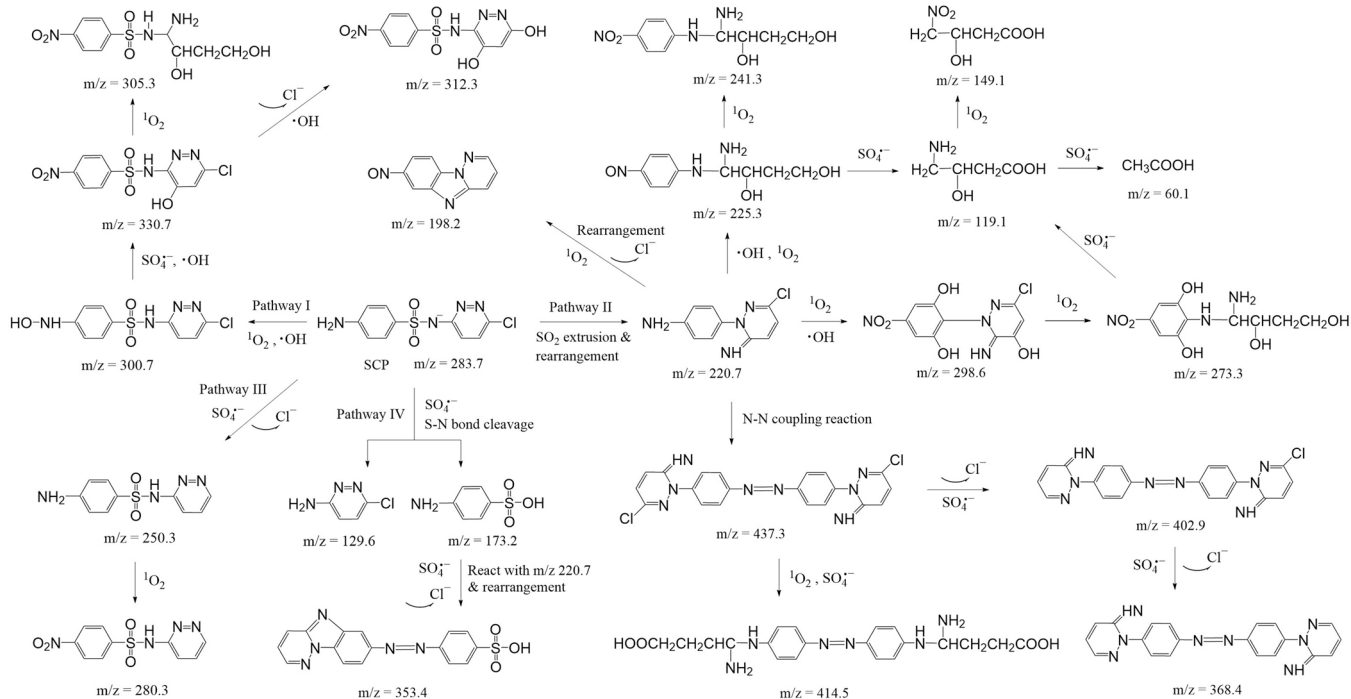


**Fig. 7.** Proposed transformation pathways for SCP degradation in CoFe<sub>2</sub>P<sub>x</sub>-1/PMS system.

transfer reaction led to the formation of *m/z* 119.1, which was further oxidized to *m/z* 149.1 and *m/z* 60.0. Meanwhile, *m/z* 198.2 was generated by the rearrangement of *m/z* 220.7 [63]. The *m/z* 437.3 was a dimerization product formed by N-N coupling reaction. Similarly, this dimer underwent the subsequent dechlorination or pyridazinyl ring-opening.

In pathway III, dechlorination and nitrification processes successively occurred with the attack of SO<sub>4</sub><sup>•-</sup> and <sup>1</sup>O<sub>2</sub> to generate *m/z* 250.3 and *m/z* 280.3, respectively. While in pathway IV, S-N bond was cleaved owing to the high electronegativity of N atom [64] to form benzenic and pyridazine derivatives. Subsequently, *m/z* 353.4 was generated through the reaction between the benzenic derivative and *m/z* 220.7.

In previous studies, the pyridazinyl ring-opening products of SCP have never been detected in reaction systems dominated by SO<sub>4</sub><sup>•-</sup> or •OH [65,66], including the CoFe<sub>2</sub>O<sub>4</sub>/PMS system [25], but were identified in that dominated by <sup>1</sup>O<sub>2</sub> [67]. Therefore, the occurrence of the pyridazinyl ring-opening products in this study once again verified the difference in activation mechanisms between CoFe<sub>2</sub>O<sub>4</sub>/PMS and CoFe<sub>2</sub>P<sub>x</sub>-1/PMS systems, i.e. the generation of <sup>1</sup>O<sub>2</sub> as discussed above. In addition, 15.3% of TOC removal was obtained in CoFe<sub>2</sub>P<sub>x</sub>-1/PMS system after reaction for 30 min, which was consistent with the various detected transformation products that have not been fully mineralized. The toxicity of the transformation products should be warranted in further investigations.

#### 4. Conclusions

In summary, CoFe<sub>2</sub>P<sub>x</sub> was synthesized, characterized and used as heterogeneous catalyst to activate PMS for SCP degradation. As expected, CoFe<sub>2</sub>P<sub>x</sub> showed desirable catalytic performance and high durability. Up to 94% of 10 mg L<sup>-1</sup> SCP was degraded within 30 min with the combination of 0.1 g L<sup>-1</sup> CoFe<sub>2</sub>P<sub>x</sub>-1 and 150 mg L<sup>-1</sup> PMS. And a particularly low concentration of leached Co ions was detected, due to the more intimate Co-Fe interaction and the surrounding of the metals by phosphorus in CoFe<sub>2</sub>P<sub>x</sub>. The CoFe<sub>2</sub>P<sub>x</sub>-1/PMS system also exhibited good performance in a variety of water matrices. Different from the previously reported common oxides/PMS systems, not only SO<sub>4</sub><sup>•-</sup> and •OH, but also O<sub>2</sub><sup>•-</sup> and <sup>1</sup>O<sub>2</sub> were identified in CoFe<sub>2</sub>P<sub>x</sub>-1/PMS system,

which was due to the generation of oxygen vacancies during phosphorization. Specifically, SO<sub>4</sub><sup>•-</sup> and <sup>1</sup>O<sub>2</sub> were the dominant ROS responsible for SCP removal, O<sub>2</sub><sup>•-</sup> promoted the generation of SO<sub>4</sub><sup>•-</sup>, whereas •OH played a minor role. Meanwhile, the oxidation pathway of SCP was proposed based on the identified intermediates including pyridazinyl ring-opening products, which was significantly different from that in common oxides/PMS systems. In general, this work extends the rational design and mechanism study of TMPs for environmental remediation.

#### CRediT authorship contribution statement

**Dingxue Gao:** Methodology, Investigation, Formal analysis, Writing – original draft. **Yirui Lu:** Investigation. **Yupeng Chen:** Validation. **Mengyuan Bao:** Validation. **Nan Xu:** Project administration, Resources, Supervision, Writing – review & editing.

#### Declaration of Competing Interest

The authors declare that they have no known competing financial interests or personal relationships that could have appeared to influence the work reported in this paper.

#### Acknowledgements

The present study was supported by the Shenzhen Fundamental Research Program (JCYJ20200109140616774, No. GXWD20201231165807007-20200810165349001), and Shenzhen Municipal Development and Reform Commission (Shenzhen Engineering Research Center for Nanoporous Water Treatment Materials).

#### Appendix A. Supporting information

Supplementary data associated with this article can be found in the online version at doi:10.1016/j.apcatb.2022.121234.

## References

- [1] P. Neta, R.E. Huie, A.B. Ross, Rate constants for reactions of inorganic radicals in aqueous solution, *J. Phys. Chem. Ref. Data* 17 (1988) 1027–1284.
- [2] G.V. Buxton, C.L. Greenstock, W.P. Helman, A.B. Ross, Critical review of rate constants for reactions of hydrated electrons, hydrogen atoms and hydroxyl radicals ( $\cdot\text{OH}/\text{O}^\bullet$ ) in aqueous solution, *J. Phys. Chem. Ref. Data* 17 (1988) 513–886.
- [3] R. Matta, S. Tlili, S. Chiron, S. Barbat, Removal of carbamazepine from urban wastewater by sulfate radical oxidation, *Environ. Chem. Lett.* 9 (2011) 347–353.
- [4] T. Olmez-Hancı, I. Arslan-Alaton, Comparison of sulfate and hydroxyl radical based advanced oxidation of phenol, *Chem. Eng. J.* 224 (2013) 10–16.
- [5] G.P. Anipsitakis, D.D. Dionysiou, Radical generation by the interaction of transition metals with common oxidants, *Environ. Sci. Technol.* 38 (2004) 3705–3712.
- [6] J. Lee, U. von Gunten, J.H. Kim, Persulfate-based advanced oxidation: critical assessment of opportunities and roadblocks, *Environ. Sci. Technol.* 54 (2020) 3064–3081.
- [7] M. Hammad, B. Alkan, A.K. Al-kamal, C. Kim, M.Y. Ali, S. Angel, H.T. A. Wiedemann, D. Klippert, T.C. Schmidt, C.W.M. Kay, H. Wiggers, Enhanced heterogeneous activation of peroxymonosulfate by Ruddlesden-Popper-type  $\text{La}_2\text{Co}_{4+8}$  nanoparticles for bisphenol A degradation, *Chem. Eng. J.* 429 (2022), 131447.
- [8] M. Kohantorabi, G. Moussavi, S. Giannakis, A review of the innovations in metal- and carbon-based catalysts explored for heterogeneous peroxymonosulfate (PMS) activation, with focus on radical vs. non-radical degradation pathways of organic contaminants, *Chem. Eng. J.* 411 (2021), 127957.
- [9] M.R. Azhar, P. Vijay, M.O. Tade, H. Sun, S. Wang, Submicron sized water-stable metal organic framework (bio-MOF-11) for catalytic degradation of pharmaceuticals and personal care products, *Chemosphere* 196 (2018) 105–114.
- [10] W.D. Oh, Z. Dong, T.T. Lim, Generation of sulfate radical through heterogeneous catalysis for organic contaminants removal: Current development, challenges and prospects, *Appl. Catal. B Environ.* 194 (2016) 169–201.
- [11] P. Hu, M. Long, Cobalt-catalyzed sulfate radical-based advanced oxidation: a review on heterogeneous catalysts and applications, *Appl. Catal. B Environ.* 181 (2016) 103–117.
- [12] G.P. Anipsitakis, D.D. Dionysiou, Degradation of organic contaminants in water with sulfate radicals generated by the conjunction of peroxymonosulfate with cobalt, *Environ. Sci. Technol.* 37 (2003) 4790–4797.
- [13] S. Ben Hammouda, F. Zhao, Z. Safaei, D.L. Ramasamy, B. Doshi, M. Sillanpaa, Sulfate radical-mediated degradation and mineralization of bisphenol F in neutral medium by the novel magnetic  $\text{Sr}_2\text{CoFeO}_6$  double perovskite oxide catalyzed peroxymonosulfate: Influence of co-existing chemicals and UV irradiation, *Appl. Catal. B Environ.* 233 (2018) 99–111.
- [14] F. Ghanbari, M. Moradi, Application of peroxymonosulfate and its activation methods for degradation of environmental organic pollutants: review, *Chem. Eng. J.* 310 (2017) 41–62.
- [15] Q. Yang, H. Choi, S.R. Al-Abed, D.D. Dionysiou, Iron-cobalt mixed oxide nanocatalysts: heterogeneous peroxymonosulfate activation, cobalt leaching, and ferromagnetic properties for environmental applications, *Appl. Catal. B Environ.* 88 (2009) 462–469.
- [16] Q. Yang, H. Choi, Y. Chen, D.D. Dionysiou, Heterogeneous activation of peroxymonosulfate by supported cobalt catalysts for the degradation of 2,4-dichlorophenol in water: The effect of support, cobalt precursor, and UV radiation, *Appl. Catal. B: Environ.* 77 (2008) 300–307.
- [17] Y. Bao, M. Tian, S.K. Lua, T.T. Lim, R. Wang, X. Hu, Spatial confinement of cobalt crystals in carbon nanofibers with oxygen vacancies as a high-efficiency catalyst for organics degradation, *Chemosphere* 245 (2020), 125407.
- [18] C. Chu, J. Yang, X. Zhou, D. Huang, H. Qi, S. Weon, J. Li, M. Elimelech, A. Wang, J. H. Kim, Cobalt single atoms on tetrapyridomacrocyclic support for efficient peroxymonosulfate activation, *Environ. Sci. Technol.* 55 (2021) 1242–1250.
- [19] C. Zhu, S. Zhao, Z. Fan, H. Wu, F. Liu, Z. Chen, A. Li, Confinement of CoP nanoparticles in nitrogen-doped yolk-shell porous carbon polyhedron for ultrafast catalytic oxidation, *Adv. Funct. Mater.* 30 (2020), 2003947.
- [20] W. Cai, Z. Zhou, X. Tan, W. Wang, W. Lv, H. Chen, Q. Zhao, Y. Yao, Magnetic iron phosphide particles mediated peroxymonosulfate activation for highly efficient elimination of sulfonamide antibiotics, *Chem. Eng. J.* 397 (2020), 125279.
- [21] C. Alexopoulou, A. Petala, Z. Frontistis, C. Drivas, S. Kennou, D.I. Kondarides, D. Mantzavinos, Copper phosphide and persulfate salt: A novel catalytic system for the degradation of aqueous phase micro-contaminants, *Appl. Catal. B Environ.* 244 (2019) 178–187.
- [22] Y. Wang, B. Kong, D. Zhao, H. Wang, C. Selomulya, Strategies for developing transition metal phosphides as heterogeneous electrocatalysts for water splitting, *Nano Today* 15 (2017) 26–55.
- [23] M. Haidar, A. Dirany, I. Sires, N. Oturan, M.A. Oturan, Electrochemical degradation of the antibiotic sulfachloropyridazine by hydroxyl radicals generated at a BDD anode, *Chemosphere* 91 (2013) 1304–1309.
- [24] Y. Du, M. Zhang, Z. Wang, Y. Liu, Y. Liu, Y. Geng, L. Wang, A self-template method for metal-organic frameworks to construct multi-shelled bimetallic phosphide hollow microspheres as highly efficient electrocatalysts for hydrogen evolution reaction, *J. Mater. Chem. A* 7 (2019) 8602–8608.
- [25] D. Gao, M. Junaid, F. Lin, S. Zhang, N. Xu, Degradation of sulphachloropyridazine sodium in column reactor packed with  $\text{CoFe}_2\text{O}_4$ -loaded quartz sand via peroxymonosulfate activation: Insights into the amorphous phase, efficiency, and mechanism, *Chem. Eng. J.* 390 (2020), 124549.
- [26] L. Zhang, X. Wang, A. Li, X. Zheng, L. Peng, J. Huang, Z. Deng, H. Chen, Z. Wei, Rational construction of macroporous CoFeP triangular plate arrays from bimetal-organic frameworks as high-performance overall water-splitting catalysts, *J. Mater. Chem. A* 7 (2019) 17529–17535.
- [27] J. Zhu, J. Wang, C. Shan, J. Zhang, L. Lv, B. Pan, Durable activation of peroxymonosulfate mediated by Co-doped mesoporous  $\text{FePO}_4$  via charge redistribution for atrazine degradation, *Chem. Eng. J.* 375 (2019), 122009.
- [28] K. Liu, C. Zhang, Y. Sun, G. Zhang, X. Shen, F. Zou, H. Zhang, Z. Wu, E.C. Wegener, C.J. Taubert, J.T. Miller, Z. Peng, Y. Zhu, High-performance transition metal phosphide alloy catalyst for oxygen evolution reaction, *ACS Nano* 12 (2018) 158–167.
- [29] T. Zeng, X. Zhang, S. Wang, H. Niu, Y. Cai, Spatial confinement of a  $\text{Co}_3\text{O}_4$  catalyst in hollow metal-organic frameworks as a nanoreactor for improved degradation of organic pollutants, *Environ. Sci. Technol.* 49 (2015) 2350–2357.
- [30] X. Li, X. Liu, C. Lin, H. Zhang, Z. Zhou, G. Fan, J. Ma, Cobalt ferrite nanoparticles supported on drinking water treatment residuals: An efficient magnetic heterogeneous catalyst to activate peroxymonosulfate for the degradation of atrazine, *Chem. Eng. J.* 367 (2019) 208–218.
- [31] G. Liu, Y. Zhou, J. Teng, J. Zhang, S. You, Visible-light-driven photocatalytic activation of peroxymonosulfate by  $\text{Cu}_2(\text{OH})\text{PO}_4$  for effective decontamination, *Chemosphere* 201 (2018) 197–205.
- [32] Z. Shi, K. Nie, Z.J. Shao, B. Gao, H. Lin, H. Zhang, B. Liu, Y. Wang, Y. Zhang, X. Sun, X.M. Cao, P. Hu, Q. Gao, Y. Tang, Phosphorus- $\text{Mo}_2\text{C}$ /carbon nanowires toward efficient electrochemical hydrogen evolution: composition, structural and electronic regulation, *Energy Environ. Sci.* 10 (2017) 1262–1271.
- [33] N. Chen, Q. Mo, L. He, X. Huang, L. Yang, J. Zeng, Q. Gao, Heterostructured  $\text{Mo-CuP/N-doped}$  carbon nanofibers as efficient electrocatalysts for hydrogen evolution reaction, *Electrochim. Acta* 299 (2019) 708–716.
- [34] H. Kim, J. Lim, S. Lee, H.H. Kim, C. Lee, J. Lee, W. Choi, Spontaneous generation of  $\text{H}_2\text{O}_2$  and hydroxyl radical through  $\text{O}_2$  reduction on copper phosphide under ambient aqueous condition, *Environ. Sci. Technol.* 53 (2019) 2198–2205.
- [35] A. Al-Anazi, W.H. Abdelraheem, C. Han, M.N. Nadagouda, L. Sygelou, M. K. Arfanis, P. Falaras, V.K. Sharma, D.D. Dionysiou, Cobalt ferrite nanoparticles with controlled composition-peroxymonosulfate mediated degradation of 2-phenylbenzimidazole-5-sulfonic acid, *Appl. Catal. B Environ.* 221 (2018) 266–279.
- [36] Q. Wang, Y. Peng, J. Fu, G.Z. Kyzas, S.M.R. Billah, S. An, Synthesis, characterization, and catalytic evaluation of  $\text{Co}_3\text{O}_4/\text{gamma-Al}_2\text{O}_3$  as methane combustion catalysts: Significance of Co species and the redox cycle, *Appl. Catal. B Environ.* 168 (2015) 42–50.
- [37] H. Li, J. Wan, Y. Ma, Y. Wang, X. Chen, Z. Guan, Degradation of refractory dibutyl phthalate by peroxymonosulfate activated with novel catalysts cobalt metal-organic frameworks: Mechanism, performance, and stability, *J. Hazard. Mater.* 318 (2016) 154–163.
- [38] R. Luo, C. Liu, J. Li, J. Wang, X. Hu, X. Sun, J. Shen, W. Han, L. Wang, Nanostructured Cop: An efficient catalyst for degradation of organic pollutants by activating peroxymonosulfate, *J. Hazard. Mater.* 329 (2017) 92–101.
- [39] D. Oh, C.S. Lee, Y.G. Kang, Y.S. Chang, Hydroxylamine-assisted peroxymonosulfate activation using cobalt ferrite for sulfamethoxazole degradation, *Chem. Eng. J.* 386 (2020), 123751.
- [40] P. Hu, M. Long, X. Bai, C. Wang, C. Cai, J. Fu, B. Zhou, Y. Zhou, Monolithic cobalt-doped carbon aerogel for efficient catalytic activation of peroxymonosulfate in water, *J. Hazard. Mater.* 332 (2017) 195–204.
- [41] S. Waclawek, H.V. Lutze, K. Grubel, V.V.T. Padil, M. Cernik, D.D. Dionysiou, Chemistry of persulfates in water and wastewater treatment: a review, *Chem. Eng. J.* 330 (2017) 44–62.
- [42] X. Lou, C. Fang, Z. Geng, Y. Jin, D. Xiao, Z. Wang, J. Liu, Y. Guo, Significantly enhanced base activation of peroxymonosulfate by polyphosphates: kinetics and mechanism, *Chemosphere* 173 (2017) 529–534.
- [43] T. Zhang, H. Zhu, J.P. Croue, Production of sulfate radical from peroxymonosulfate induced by a magnetically separable  $\text{CuFe}_2\text{O}_4$  spinel in water: efficiency, stability, and mechanism, *Environ. Sci. Technol.* 47 (2013) 2784–2791.
- [44] A. Mendoza-Garcia, H. Zhu, Y. Yu, Q. Li, L. Zhou, D. Su, M.J. Kramer, S. Sun, Controlled anisotropic growth of Co-Fe-P from Co-Fe-O nanoparticles, *Angew. Chem. -Int. Ed.* 54 (2015) 9642–9645.
- [45] P. Eyer, Effects of superoxide-dismutase on the autoxidation of 1,4-hydroquinone, *Chem. Biol. Interact.* 80 (1991) 159–176.
- [46] Y. Yang, G. Banerjee, G.W. Brudvig, J.-H. Kim, J.J. Pignatello, Oxidation of organic compounds in water by unactivated peroxymonosulfate, *Environ. Sci. Technol.* 52 (2018) 5911–5919.
- [47] X. Zhou, M. Luo, C. Xie, H. Wang, J. Wang, Z. Chen, J. Xiao, Z. Chen, Tunable S doping from  $\text{Co}_3\text{O}_4$  to  $\text{Co}_9\text{S}_8$  for peroxymonosulfate activation: distinguished radical/nonradical species and generation pathways, *Appl. Catal. B Environ.* 282 (2021), 119605.
- [48] S. Wang, Y. Liu, J. Wang, Peroxymonosulfate activation by Fe-Co-O-Codoped graphite carbon nitride for degradation of sulfamethoxazole, *Environ. Sci. Technol.* 54 (2020) 10361–10369.
- [49] G.S. Timmins, K.J. Liu, E.J.H. Bechara, Y. Kotake, H.M. Swartz, Trapping of free radicals with direct *in vivo* EPR detection: A comparison of 5,5-dimethyl-1-pyrroline-N-oxide and 5-diethoxyphosphoryl-5-methyl-1-pyrroline-N-oxide as spin traps for HO<sup>•</sup> and SO<sub>4</sub><sup>2-</sup>, *Free Radic. Biol. Med.* 27 (1999) 329–333.
- [50] E.T. Yun, J.H. Lee, J. Kim, H.D. Park, J. Lee, Identifying the nonradical mechanism in the peroxymonosulfate activation process: singlet oxygenation versus mediated electron transfer, *Environ. Sci. Technol.* 52 (2018) 7032–7042.
- [51] X. Chen, D. Vione, T. Borch, J. Wang, Y. Gao, Nano- $\text{MoO}_2$  activates peroxymonosulfate for the degradation of PAH derivatives, *Water Res.* 192 (2021), 116834, 116834–116834.

- [52] J.Y. Kim, C. Lee, D.C. Love, D.L. Sedlak, J. Yoon, K.L. Nelson, Inactivation of MS<sub>2</sub> coliphage by ferrous ion and zero-valent iron nanoparticles, Environ. Sci. Technol. 45 (2011) 6978–6984.
- [53] Y. Zhao, H. An, G. Dong, J. Feng, T. Wei, Y. Ren, J. Ma, Oxygen vacancies induced heterogeneous catalysis of peroxymonosulfate by Ni-doped AgFeO<sub>2</sub> materials: evolution of reactive oxygen species and mechanism, Chem. Eng. J. 388 (2020), 124371.
- [54] C. Li, S. Yang, R. Bian, Y. Tan, X. Dong, N. Zhu, X. He, S. Zheng, Z. Sun, Clinoptilolite mediated activation of peroxymonosulfate through spherical dispersion and oriented array of NiFe<sub>2</sub>O<sub>4</sub>: Upgrading synergy and performance, J. Hazard. Mater. 407 (2021), 124736, 124736-124736.
- [55] X. Zhou, L. Kong, Z. Jing, S. Wang, Y. Lai, M. Xie, L. Ma, Z. Feng, J. Zhan, Facile synthesis of superparamagnetic beta-CD-MnFe<sub>2</sub>O<sub>4</sub> as a peroxymonosulfate activator for efficient removal of 2,4-dichlorophenol: structure, performance, and mechanism, J. Hazard. Mater. 394 (2020), 122528.
- [56] J. Rodríguez-Chueca, E. Barahona-García, V. Blanco-Gutiérrez, L. Isidoro-García, A.J. Dos santos-García, Magnetic CoFe<sub>2</sub>O<sub>4</sub> ferrite for peroxymonosulfate activation for disinfection of wastewater, Chem. Eng. J. 398 (2020), 125606.
- [57] H. Zhang, W. Zhou, J. Dong, X.F. Lu, X.W. Lou, Intramolecular electronic coupling in porous iron cobalt (oxy)phosphide nanoboxes enhances the electrocatalytic activity for oxygen evolution, Energy Environ. Sci. 12 (2019) 3348–3355.
- [58] S. Giannakis, K.-Y.A. Lin, F. Ghanbari, A review of the recent advances on the treatment of industrial wastewaters by sulfate radical-based advanced oxidation processes (SR-AOPs), Chem. Eng. J. 406 (2021), 127083.
- [59] J.E. Grebel, J.J. Pignatello, W.A. Mitch, Effect of halide ions and carbonates on organic contaminant degradation by hydroxyl radical-based advanced oxidation processes in saline waters, Environ. Sci. Technol. 44 (2010) 6822–6828.
- [60] F. Javier Rivas, R.R. Solis, Chloride promoted oxidation of tritosulfuron by peroxymonosulfate, Chem. Eng. J. 349 (2018) 728–736.
- [61] E.T. Yun, S.W. Park, H.J. Shin, H. Lee, D.W. Kim, J. Lee, Peroxymonosulfate activation by carbon-encapsulated metal nanoparticles: Switching the primary reaction route and increasing chemical stability, Appl. Catal. B Environ. 279 (2020), 119360.
- [62] H. Chen, Y. Xu, K. Zhu, H. Zhang, Understanding oxygen-deficient La<sub>2</sub>CuO<sub>4</sub>-sperrövskite activated peroxymonosulfate for bisphenol A degradation: The role of localized electron within oxygen vacancy, Appl. Catal. B Environ. 284 (2021), 119732.
- [63] C. Chen, L. Liu, Y. Li, W. Li, L. Zhou, Y. Lan, Y. Li, Insight into heterogeneous catalytic degradation of sulfamethazine by peroxymonosulfate activated with CuCo<sub>2</sub>O<sub>4</sub> derived from bimetallic oxalate, Chem. Eng. J. 384 (2020), 123257.
- [64] J. Yao, X. Zeng, Z. Wang, Enhanced degradation performance of sulfoxazole using peroxymonosulfate activated by copper-cobalt oxides in aqueous solution: Kinetic study and products identification, Chem. Eng. J. 330 (2017) 345–354.
- [65] L. Liu, S. Lin, W. Zhang, U. Farooq, G. Shen, S. Hu, Kinetic and mechanistic investigations of the degradation of sulfachloropyridazine in heat-activated persulfate oxidation process, Chem. Eng. J. 346 (2018) 515–524.
- [66] A. Dirany, I. Sires, N. Oturan, A. Ozcan, M.A. Oturan, Electrochemical treatment of the antibiotic sulfachloropyridazine: kinetics, reaction pathways, and toxicity evolution, Environ. Sci. Technol. 46 (2012) 4074–4082.
- [67] L. Ge, P. Zhang, C. Halsall, Y. Li, C.E. Chen, J. Li, H. Sun, Z. Yao, The importance of reactive oxygen species on the aqueous phototransformation of sulfonamide antibiotics: kinetics, pathways, and comparisons with direct photolysis, Water Res. 149 (2019) 243–250.